Self-guiding and stability of intense optical beams in gases undergoing ionization

P. Sprangle, E. Esarey, and J. Krall

Beam Physics Branch, Plasma Physics Division, Naval Research Laboratory, Washington, D.C. 20375

(Received 16 May 1996)

The propagation of intense optical beams in gases undergoing ionization is analyzed. Two types of optical beam modes are considered: a fundamental Gaussian and a higher-order radially polarized beam. The propagation dynamics include the effects of diffraction, nonlinear self-focusing, and ionization. For sufficiently intense optical beams the neutral gas undergoes ionization, generating a plasma which tends to defocus the beam. An envelope equation governing the spot size for both types of beams is derived, analyzed, and solved numerically. Self-guided solutions, which result from a balancing of diffraction, plasma defocusing, and nonlinear self-focusing, are analyzed for both types of beams. These equilibrium solutions are found to be unstable due to an ionization-modulation instability for which asymptotic growth rates are obtained. A self-guided inverse Cherenkov accelerator based on the higher-order radially polarized mode is proposed and analyzed. In addition, the depletion of the optical field due to collision and ionization losses is analyzed and the attenuation length is derived. [S1063-651X(96)06810-9]

PACS number(s): 41.75.Cn, 42.25.Bs, 52.40.Nk

I. INTRODUCTION

The propagation of optical pulses in gases is relevant to a wide range of applications, such as ultrabroadband optical generators [1,2], optical harmonic generators [3,4], x-ray lasers [5], and laser-driven accelerators [6–12]. For these applications it is necessary that the optical pulse be intense and propagate extended distances. In the absence of an optical guiding mechanism the propagation distance is limited to approximately a Rayleigh (diffraction) length. At sufficiently high power and intensity the propagation distance is strongly affected by nonlinear self-focusing and ionization (plasma generation).

An optical beam propagating in a neutral gas is affected by diffraction, refraction, nonlinear self-focusing, ionization, and plasma defocusing. Self-focusing, for example, is due to the intensity-dependent part of the refractive index and occurs when the optical power is above the nonlinear focusing power [13–16]. As the beam focuses, the increased intensity results in ionization and plasma formation which tends to defocus the optical beam [9,17–21], see Fig. 1. A balance between the nonlinear focusing and plasma defocusing can result in a self-guided optical beam.

In this paper the propagation, self-guiding, and stability of two types of optical beams are analyzed. The two beams considered are a fundamental Gaussian beam of the form $E_0\exp(-r^2/r_s^2+i\psi)\hat{e}_x/2+$c.c. and a higher-order radially polarized beam of the form $E_0(\sqrt{2}r/r_s)\exp(-r^2/r_s^2+i\psi)\hat{e}_r/2+$c.c., where E_0 is the electric field amplitude, r_s is the spot size, and ψ is the phase. The results of this paper include (1) envelope equations describing the evolution of the optical beam spot size, which are derived by using the source-dependent expansion method [22,23], (2) the critical power for nonlinear self-focusing of the higher-order mode, which is four times greater than that of the fundamental Gaussian, (3) self-guided beam solutions, which result from a balance of nonlinear self-focusing and plasma defocusing, (4) the analysis of an ionization-modulation instability, which disrupts self-guided beams, (5) the evolution of the optical beam phase velocity, which is less than the speed of

light for a self-guided beam, and (6) a configuration of an inverse Cherenkov accelerator, which is based on a self-guided, radially polarized, higher-order Gaussian beam.

One important application of intense optical pulses propagating in gases is laser-driven electron accelerators, which are referred to as a class of inverse Cherenkov accelerators (ICA's) [6–9]. In the conventional ICA [6–8], the optical beam driver can consist of either a radially polarized (i) higher-order Gaussian mode or (ii) a nonideal first-order Bessel mode. Associated with these modes is an accelerating axial field peaked along the propagation direction (z axis). In general, the electron acceleration distance is limited by either the diffraction distance or the electron slippage distance. Since the optical beam in the ICA propagates in gas, the phase velocity can be less than the speed of light and controlled by varying the gas density. Electron slippage is minimized by matching the electron velocity to the phase velocity of the accelerating field. The acceleration distance, however, is still limited by the diffraction length. For a higher-order
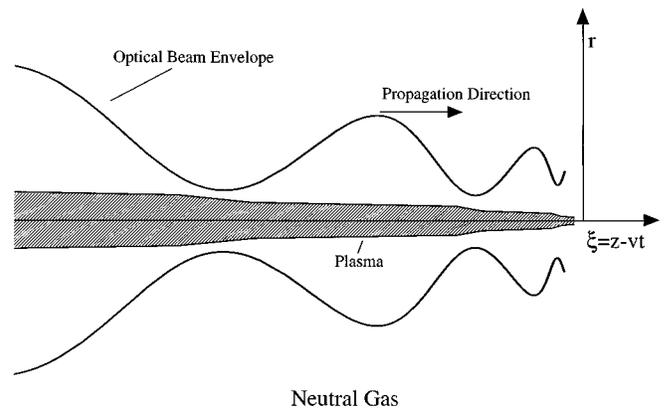
FIG. 1. Schematic of a fundamental Gaussian optical beam propagating in a gas undergoing ionization. When $P>P_{NG}$, the beam self-focuses and the intensity increases, causing ionization. Plasma is generated along the beam axis, tending to defocus the beam. Self-guiding results by balancing nonlinear self-focusing with plasma defocusing.

Gaussian mode the diffraction length is a Rayleigh length which is precisely the slippage distance in vacuum. In this case, as far as energy gain is concerned, there is essentially no advantage in introducing a gas since the effective acceleration length is limited to approximately a Rayleigh length as discussed in Sec. V. For a fixed total optical beam power, however, the energy gain in the conventional ICA can be significantly increased by using a nonideal Bessel beam, as discussed in Appendix D. To further enhance the energy gain, the ICA requires self-guiding of the optical driver [9]. Previous studies [6–8] of the ICA also neglect the intensity-dependent effects in the refractive index, i.e., nonlinear self-focusing, as well as ionization, i.e., plasma effects. We propose and analyze a self-guided ICA configuration that operates at laser powers near the nonlinear self-focusing power and at intensities high enough to slightly ionize the gas.

Another possible application of intense optical beams in gases is the generation of ultrabroadband [1,2] or harmonic radiation [3,4]. A short-pulse optical beam propagating in a nonlinear medium will, among other things, undergo self-phase modulation [13–16] which results in frequency broadening. Since the degree of frequency broadening increases with both propagation distance and optical intensity, the self-guiding of a short optical beam may be well suited for ultrabroadband radiation generation. A self-guided Gaussian beam may have application to harmonic generation [3,4], since the propagation medium consists mainly of a neutral gas and a very narrow plasma column along the axis. The harmonics could be guided by the driving optical beam and phase matching may be achieved by introducing a background plasma.

This paper is organized as follows. The propagation model is presented in Sec. II, and includes discussions of the wave equation in a gas undergoing ionization, the linear and nonlinear polarization, plasma generation, the reduced wave equation, photoionization, the solution of the wave equation using the source-dependent expansion method, and the resulting equations describing the evolution of the envelope, amplitude, and phase of the optical beam. The propagation of a fundamental Gaussian beam is examined analytically and numerically in Sec. III, including the envelope equation, self-guided solutions, and the stability, i.e., the ionization-modulation instability. Numerical results on the propagation of the fundamental Gaussian beam are also presented in Sec. III. The propagation of a higher-order radially polarized beam is analyzed in Sec. IV, including the envelope equation, self-guided solutions, and the stability. Numerical results on the propagation of the higher-order radially polarized beam are also presented in Sec. IV. The analysis of a self-guided inverse Cherenkov accelerator is presented in Sec. V. Attenuation of the optical beam due to electron collisions and ionization losses is analyzed in Sec. VI. Section VII contains a discussion and summary. This paper also includes four Appendices discussing (A) photoionization rates, (B) electron collision frequencies, (C) radiative and collision losses on accelerated electrons, and (D) inverse Cherenkov acceleration with Bessel (axicon) beams.

II. PROPAGATION MODEL

The propagation of intense optical beams in gases is affected by a combination of diffraction, refraction, and ion-

ization. The refractive index of a gas generally has an intensity-dependent part [13–16], $n = n_0 + n_2 I$, where n_0 is the linear refractive index, n_2 is the nonlinear refractive index, and I is the intensity of the optical beam. Generally, n_2 is positive and results in self-focusing of the optical beam if the power is greater than the nonlinear focusing power. The nonlinear focusing (critical) power for a fundamental Gaussian beam [13–16] is $P_{NG} = \lambda^2/(2\pi n_0 n_2)$, where λ is the vacuum wavelength. As the beam self-focuses the peak intensity increases, resulting in ionization and the generation of a plasma. In the region of the plasma the refractive index is $n(r) = n_0 + n_2 I - \omega_p^2(r)/2\omega^2$, where $\omega_p = (4\pi q^2 n_p/m)^{1/2}$ is the plasma frequency, n_p is the plasma density, and $\omega = 2\pi c/\lambda$ is the frequency of the optical beam. The local decrease in the refractive index due to the plasma tends to defocus the optical beam [9,17–21]. If diffraction, self-focusing due to n_2, and defocusing due to plasma generation are properly balanced, a self-guided optical beam can be formed and propagated over extended distances, i.e., many vacuum Rayleigh lengths [9,20,21].

Our propagation model includes a number of assumptions. The short-pulse optical beam is assumed to be adequately described by a single source-dependent Laguerre-Gaussian mode, which is a superposition of many vacuum Laguerre-Gaussian modes. The model is not valid when the optical power greatly exceeds the nonlinear focusing power, since the beam is expected to filament into higher-order modes. Ionization is considered in the high field limit [24–28] (Keldysh parameter less than unity) and is modeled by the tunneling ionization rate; see Appendix A. The attenuation of the optical beam due to ionization and collisional losses is estimated and found to be small enough to neglect. The nonlinear polarization field of the gas is included to third order in the optical field whereas the plasma current is included to first order.

A. Wave equation in gas undergoing ionization

The dynamics of optical beams propagating in a gas undergoing ionization is governed by the wave equation,

$$(\nabla^2 - c^{-2}\partial^2/\partial t^2)\mathbf{E} = 4\pi c^{-2}(\partial^2\mathbf{P}/\partial t^2 + \partial\mathbf{J}_p/\partial t), \quad (1)$$

where $\mathbf{E}$ is the electric field of the optical beam, $\nabla^2 = \nabla_\perp^2 + \partial^2/\partial z^2$, z is the axial propagation direction, $\mathbf{P}$ is the polarization field associated with the gas, and $\mathbf{J}_p$ is the plasma current density associated with the ionized gas. In obtaining Eq. (1) we have neglected a small source term proportional to the gradient of the plasma density.

1. Linear and nonlinear polarization

The polarization field can arise from a number of processes; these include electronic polarization, molecular orientation, electrostriction, saturated absorption, and thermal effects [13–16]. In the present paper we will be concerned with changing the refractive index on a fast time scale, typically less than 10^{-12} sec. On this time scale the electronic polarization is the dominant contribution to the nonlinear refractive index and is due to the optical field modifying the atomic electronic distribution.

In the simple Lorentz model [13–16] of the atom the electrons are assumed to consist of a charge distribution oscillat-

ing in an effective potential. Nonlinearities in the effective potential result in a field-dependent refractive index for the medium. In the following description of the polarization field only isotropic matter having ensemble-averaged inversion symmetry, i.e., centrosymmetric ensemble-averaged effective potentials, will be considered. This includes all liquids, gases, amorphous solids, as well as many crystals.

The electric polarization field is defined by $\mathbf{P} = q n_n \mathbf{x}_d$, where q is the electronic charge, n_n is the density of atoms or molecules and $\mathbf{x}_d$ is the displacement of the electronic distribution from equilibrium due to the optical field. The polarization field in the classical single resonant frequency model is given by [13–16]

$$\partial^2 \mathbf{P}/\partial t^2 + \Omega_R^2 \mathbf{P} - \Omega_1^2 (\mathbf{P} \cdot \mathbf{P}/P_n^2) \mathbf{P} + 2\Gamma \partial \mathbf{P}/\partial t = (q^2 n_n/m) \mathbf{E}, \quad (2)$$

where Ω_R is the characteristic resonant frequency of the electronic distribution, Ω_1 is a constant associated with the nonlinear, i.e., nonparabolic, nature of the effective potential, P_n is a normalizing polarization field amplitude, and Γ is a damping term. Equation (2) is an accurate description for the polarization field when the optical frequency is far from the resonant frequencies. Typically, the resonant frequency Ω_R is in the ultraviolet regime, $\Omega_R \gg \omega$. The polarization field given by Eq. (2) contains dispersion, damping, and third-order nonlinear effects.

In the limit where (i) dispersive effects are weak (far from resonance, $\Omega_R \gg \omega$), (ii) damping effects can be neglected ($\Gamma \ll \omega$), and (iii) the nonlinear term in Eq. (2) is small ($\Omega_1^2 \mathbf{P}^2/P_n^2 \ll \Omega_R^2$), the polarization field can be approximated by

$$\mathbf{P} = \chi^{(1)} \mathbf{E} + \chi^{(3)} \langle \mathbf{E} \cdot \mathbf{E} \rangle \mathbf{E} = (1/4\pi)(n_0^2 - 1 + 2n_0 n_2 I) \mathbf{E}, \quad (3)$$

where $\chi^{(1)} = q^2 n_n/(m \Omega_R^2) \ll 1$ is the constant linear susceptibility, $\chi^{(3)} = (\Omega_1/\Omega_R)^2 (\chi^{(1)})^3/P_n^2 \ll \chi^{(1)}/\langle \mathbf{E} \cdot \mathbf{E} \rangle$ is the constant third-order susceptibility of the neutral gas, the brackets $\langle \rangle$ denote a time average, $n_0 = (1 + 4\pi\chi^{(1)})^{1/2}$ is the linear refractive index of the neutral gas, $n_2 = (8\pi^2/n_0^2 c) \chi^{(3)}$ is the nonlinear component of the refractive index, $I = (c/4\pi) n_0 \langle \mathbf{E} \cdot \mathbf{E} \rangle$ is the intensity, and $|n_2 I| \ll n_0$ has been assumed.

2. Plasma generation

The ionization of the background gas by the optical beam results in the generation of plasma electrons. The plasma current density is given by $\mathbf{J}_p = q n_p \mathbf{v}_p$, where n_p and $\mathbf{v}_p$ are the plasma density and fluid velocity respectively. To lowest order in $\mathbf{v}_p$, the continuity and fluid velocity equations are

$$\partial n_p/\partial t + \nabla \cdot (n_p \mathbf{v}_p) = S, \quad (4a)$$

$$m n_p \partial \mathbf{v}_p/\partial t = q n_p \mathbf{E} - m \mathbf{v}_p S, \quad (4b)$$

where S is the plasma source term proportional to the ionization rate, $\mathbf{E}$ is the optical electric field, the $\mathbf{v}_p \times \mathbf{B}$ force and thermal effects are neglected in Eq. (4b), and the electrons are assumed to be created with zero velocity when ionized. Combining Eqs. (4a) and (4b), and keeping terms to lowest order in $\mathbf{v}_p$, the plasma current density is given by [29–31]

$$\partial \mathbf{J}_p/\partial t = (\omega_p^2/4\pi) \mathbf{E}, \quad (5)$$

where $\omega_p = (4\pi q^2 n_p/m)^{1/2}$ is the electron plasma frequency. The evolution of the plasma density depends on the photoionization rate and is discussed later. In obtaining Eq. (5), nonlinear and collisional effects (see Appendix B) have been neglected. Ionization and collisional losses are analyzed in Sec. VI and found to be small. Nonlinear plasma effects are small compared to the nonlinear neutral gas effects, which are represented by the term $n_2 I$ in Eq. (3). The magnitude of nonlinear plasma effects compared to nonlinear neutral gas effects is approximately given by the ratio of the critical power for relativistic focusing [11,32] to the nonlinear focusing power and is found to be negligibly small.

3. Reduced wave equation

The propagation of the optical beam is described by Eqs. (1), (3), and (5) together with the tunneling ionization model discussed in Sec. II B. To proceed with the analysis, it is convenient to transform from the (z, t) coordinates to the (ξ, η) coordinates, where $\xi = z - vt$ and $\eta = z$. For a beam propagating in the positive z direction with group velocity v, ξ is the distance behind the front ($\xi = 0$) of the optical beam and η is the propagation distance. In these new coordinates, the optical field has the form

$$\mathbf{E} = \hat{\mathbf{E}} \exp(ik\xi)/2 + \text{c.c.}, \quad (6)$$

where $\hat{\mathbf{E}}(r, \theta, \xi, \eta)$ is the complex amplitude and is a slowly varying function of ξ and η, $k = \omega/v$, $\omega = 2\pi c/\lambda$ is the optical frequency, λ is the vacuum wavelength, and c.c. denotes the complex conjugate. In the (ξ, η) coordinates, Eq. (1) can be written in the paraxial approximation as

$$(\nabla_\perp^2 + 2ik\partial/\partial\eta)\hat{\mathbf{E}} = K^2 \hat{\mathbf{E}}, \quad (7)$$

where K^2 is given by

$$K^2 = k_p^2 - 2k^2(n_2/n_0)I. \quad (8)$$

In obtaining Eq. (7) we used the transformations $\partial/\partial z = \partial/\partial\xi + \partial/\partial\eta$ and $\partial/\partial t = -v\partial/\partial\xi$. The linear group velocity as well as the linear phase velocity is $v = \omega/k = c/n_0$. The paraxial approximation implies that K^2 is small compared to k^2. In the absence of the nonlinear index ($n_2 = 0$), the paraxial approximation requires that the plasma density be small compared to the critical density, $\omega_p^2 < \omega^2$.

B. Photoionization model

Ionization can occur by electron collisional processes [33–35] or by the intense optical fields directly [24–28], i.e., photoionization. In the absence of collisions or for laser pulses short compared to a collision time, photoionization is the dominant process. Photoionization can take place by either tunneling or multiphoton processes, see Appendix A. These regimes are characterized by the Keldysh parameter $\gamma_k = (U_I/\epsilon_{os})^{1/2}$, where U_I is the ionization energy and $\epsilon_{os} = (1/2)m(q|\hat{\mathbf{E}}|/m\omega)^2$ is the electron oscillation energy. The low field limit ($\gamma_k > 1$) corresponds to the multiphoton ion-

ization regime, whereas the high field limit ($\gamma_k < 1$) corresponds to the tunneling ionization regime.

The evolution of plasma density in Eq. (4a) is given by

$$\partial n_p / \partial t = (n_{n0} - n_p) W(|\hat{\mathbf{E}}|), \qquad (9)$$

where n_{n0} is the initial neutral density, $W(|\hat{\mathbf{E}}|)$ is the ionization rate, and the convection term $\nabla \cdot (n_p \mathbf{v}_p)$ is neglected. For a linearly polarized optical field, the ionization rate in the tunneling limit ($\gamma_k < 1$) is given by [24–28]

$$W(|\hat{\mathbf{E}}|) = 4(3/\pi)^{1/2} \Omega_0 (\tilde{U}_I)^{7/4} (E_H / |\hat{\mathbf{E}}|)^{1/2}$$
$$\times \exp[-\tfrac{2}{3}(\tilde{U}_I)^{3/2} E_H / |\hat{\mathbf{E}}|], \qquad (10)$$

where $\Omega_0 = \alpha_f c / a_0 = 4.1 \times 10^{16}$ sec^{-1} is the characteristic atomic frequency, $\alpha_f = 1/137$ is the fine structure constant, $a_0 = 5.3 \times 10^{-9}$ cm is the Bohr radius, $\tilde{U}_I = U_I / U_H$, U_I is the ionization energy in eV, $U_H = 13.6$ eV is the ionization energy of hydrogen, $|\hat{\mathbf{E}}|$ is the magnitude of the optical field, and $E_H = |q| / a_0^2 = 5.2$ GV/cm is the atomic field of hydrogen. The intensity of a linearly polarized Gaussian optical beam in vacuum, with a peak field equal to E_H, is $I = (c/8\pi) E_H^2 \approx 3.6 \times 10^{16}$ W/cm^2. Equation (9) assumes that the gas is at most singly ionized. The solution of Eq. (9) yields

$$k_p^2 = k_{p0}^2 \left[1 - \exp\left(-(n_0/c) \int_\xi^0 W(|\hat{\mathbf{E}}|) d\xi' \right) \right], \qquad (11)$$

where we have set $\partial / \partial t = -(c/n_0) \partial / \partial \xi$ in Eq. (9), ξ is defined in the region $\xi \leq 0$, $\xi = 0$ corresponds to the front of the beam, and $ck_{p0} = \omega_{p0} = (4\pi q^2 n_{n0}/m)^{1/2}$ is the plasma frequency associated with the initial neutral gas density. For low levels of ionization, i.e., $n_p \ll n_{n0}$, Eq. (11) reduces to

$$k_p^2 = k_{p0}^2 (n_0/c) \int_\xi^0 W(|\hat{\mathbf{E}}|) d\xi'. \qquad (12)$$

The weakly ionized limit is sufficient to describe self-guiding of optical beams, since it will be shown that in the highly ionized limit $n_p \simeq n_{n0}$ there is no matched beam solution. The expression in Eq. (8) can be written as

$$K^2 = k_{p0}^2 (n_0/c) \int_\xi^0 W(|\hat{\mathbf{E}}|) d\xi' - 2k^2 (n_2/n_0) I. \qquad (13)$$

C. Source-dependent expansion method

The following analysis is based on the source-dependent expansion (SDE) method developed in Ref. [22]. The SDE is a powerful method for solving the paraxial wave equation for optical beams propagating in nonlinear media. In the SDE method, the optical beam is expanded in a complete set of source-dependent orthogonal Laguerre-Gaussian functions. These functions are implicitly functions of the propagation distance, η, through the optical beam parameters, i.e., spot size, wavefront curvature, amplitude, and phase. The optical beam can be described by four coupled first-order differential equations for the beam parameters in the variable η. In general, $\hat{\mathbf{E}}$ can be written in terms of a complete set of Laguerre-Gaussian functions, i.e., source-dependent modes,

$$\hat{\mathbf{E}} = \sum_{m,p} [a_{m,p} \cos(p\theta) \hat{\mathbf{e}}_\perp + b_{m,p} \sin(p\theta) \hat{\mathbf{e}}'_\perp] D_m^p(\chi), \qquad (14)$$

where $m, p = 0, 1, 2, \ldots$, $a_{m,p}(\eta)$ and $b_{m,p}(\eta)$ are complex coefficients and are functions of η, $\hat{\mathbf{e}}_\perp$ and $\hat{\mathbf{e}}'_\perp$ denote transverse unit vectors defining the polarization, $D_m^p(\chi) = \chi^{p/2} L_m^p(\chi) \exp[-(1 - i\alpha)\chi/2]$, $\chi = 2r^2/r_s^2$, $r_s(\eta)$ is real and denotes the spot size, $\alpha(\eta) = kr_s^2/(2R_c)$ is real, R_c is the radius of curvature associated with the wave front, and L_m^p is an associated Laguerre polynomial, e.g., $L_0^p(\chi) = 1$ and $L_1^p(\chi) = 1 + p - \chi$. The representation in Eq. (14) forms a complete set and can be used to represent an arbitrary optical beam.

To proceed with the SDE analysis we substitute Eq. (14) into the paraxial wave equation, Eq. (7), carry out the indicated differential operations, perform the operation

$$\int_0^{2\pi} (\cos(p'\theta), \sin(p'\theta)) d\theta / 2\pi$$

on both sides of the equation, multiply both sides by $[D_m^p(\chi)]^*$, and finally integrate over χ from 0 to ∞. The algebraic details can be found in Ref. [22]. The resulting equation for $a_{m,p}$ is

$$\left(\frac{\partial}{\partial \eta} + A_{m,p} \right) a_{m,p} - imB a_{m-1,p} - i(m+p+1) B^* a_{m+1,p}$$
$$= -iF_{m,p}, \qquad (15)$$

where

$$A_{m,p} = \dot{r}_s / r_s + i(2m + p + 1)$$
$$\times [(1 + \alpha^2)/(kr_s^2) - \alpha \dot{r}_s / r_s + \dot{\alpha}/2], \qquad (16a)$$

$$B(\eta) = -\alpha \dot{r}_s / r_s - (1 - \alpha^2)/(kr_s^2) + \dot{\alpha}/2$$
$$-i[\dot{r}_s / r_s - 2\alpha/(kr_s^2)], \qquad (16b)$$

$$F_{m,p} = \frac{1}{2\pi k} \frac{m!}{(m+p)!} \int_0^{2\pi} d\theta \int_0^\infty d\chi \, K^2(\chi, \theta, \eta)$$
$$\times \hat{\mathbf{E}}(\chi, \theta, \eta) \cdot \hat{\mathbf{e}}_\perp [D_m^p(\chi)]^* \cos(p\theta)/(1 + \delta_{p,0}), \qquad (16c)$$

$\delta_{p,p'}$ is the Kronecker delta, the dot denotes the operator $\partial / \partial \eta$, and the asterisk denotes the complex conjugate. The equation for $b_{m,p}$ is identical to the one for $a_{m,p}$ except in the expression for $F_{m,p}$, $\cos(p\theta)/(1 + \delta_{p,0})$ is replaced with $\sin(p\theta)$. In obtaining Eq. (15) a number of identities associated with Laguerre-Gaussian functions were used, including the orthogonality relation

$$\int_0^\infty D_m^p(\chi) (D_n^p(\chi))^* d\chi = \frac{(n+p)!}{n!} \delta_{m,n}.$$

Equation (15), together with the definitions in Eqs. (16), describes the evolution of the various source-dependent Laguere-Guassian modes. However, Eq. (15) is underdeter-

mined since there are more unknowns than equations. An additional constraint, i.e., a specification of the function $B(\eta)$, is necessary to solve Eq. (15). The individual source-dependent modes in Eq. (14) are functions of the spot size, $r_s(\eta)$, wavefront radius of curvature, $R_c = kr_s^2/(2\alpha)$, amplitude and phase, $a_{m,p}$. Since $B(\eta)$ is also a function of r_s and α, the evolution of the source-dependent mode is governed by the particular choice for the function B. For example, if we choose $B(\eta) = 0$, we recover the conventional vacuum modes. In general, expansion in terms of the vacuum modes ($B = 0$) requires many modes to accurately describe a guided optical beam over distances of many Rayleigh lengths. A more appropriate choice for $B(\eta)$ will depend on the particular problem under consideration and will be discussed later.

The dynamics of (i) a fundamental Gaussian beam and (ii) a higher-order radially polarized axially symmetric beam will be considered. The fundamental Gaussian beam is described by the mode numbers $m = 0$ and $p = 0$, whereas the higher-order radially polarized axially symmetric beam is described by the mode numbers $m = 0$ and $p = 1$. The analysis can be significantly simplified by setting $m = 0$.

In the following, it is assumed that the dynamics of the optical beam can be adequately described by the behavior of a single source-dependent mode, e.g., the $m = 0$, $p = 0$ mode for the fundamental Gaussian and the $m = 0$, $p = 1$ mode for the higher-order beam. In the SDE method, it is assumed that the coupling to, as well as the amplitude of, the higher-order source-dependent modes are small. In fact, an optimal choice for the function $B(\eta)$ can be determined from Eq. (15) by requiring that the higher-order source-dependent modes, i.e., $m \geq 1$, are small. Since, for the cases under consideration, $|a_{0,p}| \gg |a_{m,p}|$ for $m \geq 1$, it is clear from Eq. (15) (with $m = 1$) that the optimal choice for B is

$$B = F_{1,p}/a_{0,p}, \qquad (17)$$

where B and $F_{1,p}$ are given by Eqs. (16b) and (16c), respectively. With this choice for B, Eq. (15) (with $m = 0$) yields

$$\left(\frac{\partial}{\partial \eta} + A_{0,p}\right) a_{0,p} = -iF_{0,p}, \qquad (18)$$

where $A_{0,p}$ and $F_{0,p}$ are given by Eqs. (16). Equations (17) and (18) completely determine the evolution of the source-dependent optical beam mode. Substituting Eqs. (16a) and (16b) into Eqs. (17) and setting $a_{0,p} = E_0 \exp(i\theta_0)$, where E_0 and θ_0 are real and denote the field amplitude and phase, we obtain [22]

$$\dot{\theta}_0 + (1+p)[(1+\alpha^2)/(kr_s^2) - \alpha \dot{r}_s/r_s + \dot{\alpha}/2] = -G, \quad (19a)$$

$$\alpha \dot{r}_s/r_s + (1-\alpha^2)/(kr_s^2) - \dot{\alpha}/2 = -H, \qquad (19b)$$

$$\dot{r}_s/r_s - 2\alpha/(kr_s^2) = 0, \qquad (19c)$$

$$\dot{E}_0/E_0 + \dot{r}_s/r_s = 0, \qquad (19d)$$

where $G = F_{0,p}/a_{0,p}$ and $H = F_{1,p}/a_{0,p}$ are real. The source functions G and H are given by

$$\left.\begin{matrix} G \\ H \end{matrix}\right\} = \frac{1}{2k} \int_0^\infty d\chi \; K^2(\chi,\eta) \chi^p \exp(-\chi) \left\{\begin{matrix} 1 \\ 1 - \chi/(1+p) \end{matrix}\right\}, \qquad (20)$$

and K^2 is given by Eq. (13).

D. Envelope, amplitude, and phase of optical beam

Equations (19b) and (19c) can be combined to form an envelope equation for the optical beam

$$\partial^2 r_s/\partial \eta^2 - 4(1 + kr_s^2 H)/(k^2 r_s^3) = 0. \qquad (21)$$

In addition, the amplitude, phase, curvature, and axial phase velocity v_{ph} of the optical beam are given, respectively, by

$$\partial(E_0 r_s)/\partial \eta = 0, \qquad (22a)$$

$$\dot{\theta}_0 = -(1+p)[2/(kr_s^2) + H] - G, \qquad (22b)$$

$$\alpha = kr_s^2/(2R_c) = k\dot{r}_s r_s/2, \qquad (22c)$$

and

$$v_{ph} \simeq (1 - \dot{\theta}_0/k)c/n_0, \qquad (22d)$$

where $|\dot{\theta}/k| \ll 1$ was assumed in Eq. (22d). Note that Eq. (22a) implies that the optical power, which is proportional to $(E_0 r_s)^2$, is a conserved quantity, consistent with the paraxial wave equation when K^2 is real.

For propagation in vacuum ($n_0 = 1$) the solution of Eqs. (19a)–(19d) yield the conventional vacuum modes [15,36]. In vacuum, the source terms vanish, i.e., $G = H = 0$, and the solutions are characterized by a spot size $r_s = r_{s0}(1 + \eta^2/Z_{R0}^2)^{1/2}$, r_{s0} is the minimum spot size at the focal point $\eta = z = 0$, $Z_{R0} = kr_{s0}^2/2$ is the Rayleigh length, $\alpha = \eta/Z_{R0} = z/Z_{R0}$, a wave front radius of curvature $R_c = z(1 + Z_{R0}^2/z^2)$, a phase factor $\theta_0 = \theta_0(\eta = 0) - (1+p)\tan^{-1}\alpha$, an amplitude $E_0 = E_0(\eta = 0)r_{s0}/r_s$, and a phase velocity $v_{ph}/c = 1 + 2(1+p)/k^2 r_s^2$.

III. FUNDAMENTAL GAUSSIAN BEAM PROPAGATION

We first consider the dynamics of a fundamental Gaussian optical beam propagating in a gas undergoing ionization. The fundamental Gaussian beam, polarized in the x direction, is obtained by setting $m = p = 0$ and $\hat{e}_\perp = \hat{e}_x$ in Eq. (14). Using Eq. (14) and Eq. (6) the Gaussian beam is given by

$$\mathbf{E} = E_0 \exp(-r^2/r_s^2 + i\psi)\hat{e}_x/2 + \text{c.c.}, \qquad (23)$$

where $\psi = k\xi + \theta_0 + \alpha r^2/r_s^2$ and the functions E_0, θ_0, α, and r_s are given by Eqs. (21) and (22) with $p = 0$. From Eq. (22a), $E_0(\xi,\eta) = E_0(\xi,\eta = 0)r_s(\xi,\eta = 0)/r_s(\xi,\eta)$, where $E_0^2(\xi,\eta = 0)r_s^2(\xi,\eta = 0)$ is proportional to the optical beam power $P(\xi)$. The intensity and power associated with the Gaussian beam in a medium of refractive index n_0 are, respectively,

$$I = (c/4\pi)\langle \mathbf{E} \times \mathbf{B}\rangle \cdot \mathbf{e}_z = I_p \exp(-\chi), \qquad (24a)$$

$$P = (\pi/2)r_s^2 \int_0^\infty d\chi \; I(\chi) = (\pi/2)r_s^2 I_p, \qquad (24b)$$

where $I_p = (cn_0/8\pi)E_0^2$ is the peak intensity along the axis, $r = 0$, and $\langle \rangle$ denotes time averaging.

To determine the optical beam dynamics from Eqs. (21) and (22) the source functions $G(\eta)$ and $H(\eta)$ in Eq. (20) are evaluated with $p = 0$. Substituting Eq. (13) into Eq. (20) and integrating over χ we obtain

$$\left.\begin{array}{c} G \\ H \end{array}\right\} = -(k/2)\left[(n_2/n_0)I_p\left\{\begin{array}{c} 1 \\ 1/2 \end{array}\right\} - (k_{p0}/k)^2\left\{\begin{array}{c} \sigma_{G1} \\ \sigma_{G2} \end{array}\right\}\right], \quad (25)$$

where the functions σ_{G1}, σ_{G2} represent filling factors which are essentially the ratio of the cross-sectional area of the plasma to that of the optical mode times the normalized plasma density. The functions σ_{G1} and σ_{G2} are given by

$$\left.\begin{array}{c} \sigma_{G1} \\ \sigma_{G2} \end{array}\right\} = \int_0^\infty d\chi (k_p/k_{p0})^2 \times \left\{\begin{array}{c} 1 \\ 1-\chi \end{array}\right\} \times \exp(-\chi). \quad (26)$$

Ionization is maximum where the optical field amplitude is maximum, i.e., at $r = 0$ for the fundamental Gaussian beam. Since the tunneling ionization rate $W(|\hat{\mathbf{E}}|)$ depends exponentially on the field amplitude, the radial profile of the plasma density will be highly peaked about the axis $r = 0$. Equation (26) can be simplified by expanding the integrand about $r = 0$, which gives $\sigma_{G1} = \sigma_{G2} = \sigma_G$, where

$$\sigma_G \simeq \int_\xi^0 d\xi' K_G(\xi')[r_s^2(\xi')/r_s^2(\xi)]\int_0^\infty d\chi$$

$$\times \exp[-b_G(\xi')\chi/2]$$

$$\simeq 2\int_\xi^0 d\xi' K_G(\xi')[r_s^2(\xi')/r_s^2(\xi)]/b_G(\xi'), \quad (27)$$

and

$$K_G(\xi) = 4n_0(3/\pi)^{1/2}(\Omega_0/c)(\widetilde{U}_I)^{7/4}[\widetilde{E}_0(\xi)]^{-1/2}$$

$$\times \exp[-b_G(\xi)], \quad (28a)$$

$$b_G(\xi) = (2/3)(\widetilde{U}_I)^{3/2}/\widetilde{E}_0(\xi), \quad (28b)$$

and $\widetilde{E}_0 = E_0/E_H$. The quantities K_G, b_G, r_s, and E_0 are functions of ξ and η, whereas the power $P \sim r_s^2 E_0^2$ is only a function of ξ as implied by Eq. (22a).

A. Envelope equation for the Gaussian beam

Using Eqs. (25)–(28), the envelope equation for the Gaussian beam in Eq. (21) becomes

$$\partial^2 R/\partial\eta^2 = Z_{R0}^{-2}R^{-3}(1 - P/P_{NG} + \tfrac{1}{2}r_s^2 k_{p0}^2\sigma_G), \quad (29)$$

where r_{s0} is constant, $Z_{R0} = kr_{s0}^2/2 = \pi n_0 r_{s0}^2/\lambda$ is the Rayleigh length associated with the spot size r_{s0}, $R = r_s/r_{s0}$ is the normalized spot size, $P = (\pi/2)I_p r_s^2$ is the total power, and $P_{NG} = \lambda^2/(2\pi n_0 n_2)$ is the nonlinear focusing power for the Gaussian beam [13–16]. The terms on the right-hand side of Eq. (29) denote, respectively, vacuum diffraction, nonlinear focusing, and plasma defocusing.

In the absence of ionization ($\sigma_G = 0$) the envelope equation in Eq. (29) has the solution

$$r_s = r_{s0}[1 + (1 - P/P_{NG})(\eta/Z_{R0})^2]^{1/2}, \quad (30)$$

where $\dot{r}_s$ is assumed to be zero at $\eta = 0$. For $P < P_{NG}$ the optical beam diffracts with an effective Rayleigh length given by

$$Z_R = (1 - P/P_{NG})^{-1/2}Z_{R0}. \quad (31)$$

For $P = P_{NG}$, diffractive spreading balances nonlinear focusing and a matched self-guided beam can, in principle, be obtained. However, small changes away from $P = P_{NG}$ will result in loss of equilibrium. For $P > P_{NG}$ the optical beam self-focuses. In the absence of ionization the beam focuses down to zero spot size with a focal length given by

$$L_f = (P/P_{NG} - 1)^{-1/2}Z_{R0}, \quad (32)$$

However, as the beam focuses the intensity on axis increases resulting in ionization and plasma defocusing, as is described by Eq. (29).

B. Self-guided Gaussian beam

In the presence of ionization, self-guided solutions to Eq. (29) can be obtained. The condition for a self-guided beam, i.e., $\partial^2 R/\partial\eta^2 = 0$, is

$$P/P_{NG} - 1 = k_{p0}^2 r_s^2 \sigma_G/2 \geqslant 0. \quad (33)$$

Upon taking the derivative of this expression with respect to ξ and using Eq. (27) we find that for a self-guided beam

$$\partial P/\partial\xi = -k_{p0}^2 P_{NG}r_s^2(\xi)K_G(\xi)/b_G(\xi) = -Ph_G(\xi), \quad (34)$$

where

$$h_G = 16k_{p0}^2(P_{NG}/cn_0)K_G(\xi)/[E_0^2(\xi)b_G(\xi)],$$

is a function of $E_0(\xi)$. The solution of Eq. (34) yields the self-guided optical Gaussian beam power as a function of ξ,

$$P(\xi) = P_{NG}\exp\left(\int_\xi^0 h_G(\xi')d\xi'\right). \quad (35)$$

Equation (33) or (35) describes a family of equilibrium solutions, i.e., there are various equilibrium profiles $P(\xi)$, $E_0(\xi)$, and $r_s(\xi)$ which satisfy these equations. For example, if an equilibrium is chosen such that $E_0(\xi)$ is constant along the optical beam, then h_G is constant and Eq. (35) implies $P(\xi) = P_{NG}\exp(-\xi h_G)$ and the spot size profile is given by $r_s^2(\xi) = (16/cn_0)P(\xi)/E_0^2$. Behind the beam front, $\xi < 0$, the optical beam power and plasma density increase such that the nonlinear self-focusing term and the plasma defocusing term remain balanced. Other types of equilibria can be found, for example, one in which $r_s(\xi)$ is constant.

C. Stability of the Gaussian beam

In this section, the self-guided beam equilibrium described above is shown to be inherently unstable, i.e., the beam will undergo what we refer to as an ionization-modulation (IM) instability. The IM instability is due to varying degrees of ionization along the beam and results in the modulation of the beam envelope and the disruption of the back of the beam. To examine the stability of the self-guided beam equilibrium, the envelope equation, Eq. (29), is

expanded about the equilibrium solution. The perturbations $\delta r(\xi,\eta)$ and $\delta E(\xi,\eta)$ are such that $r_s(\xi) + \delta r$ and $E_0(\xi) + \delta E$ denote the perturbed spot size and optical field amplitude, respectively. Furthermore, since the optical beam power within the paraxial approximation is nonevolving, i.e., independent of η, the perturbations δr and δE are related by $\delta r = -(r_s/E_0)\delta E$. Expansion of the envelope equation, Eq. (29), yields

$$\partial^2 \delta r/\partial \eta^2 = -\frac{4k_{p0}^2}{k^2 r_s^3(\xi)} \int_\xi^0 d\xi' K_G(\xi') r_s(\xi') \delta r(\xi',\eta), \quad (36)$$

where $b_G \gg 1$ has been assumed (typically the case). For the special case of an equilibrium with a constant spot size, $r_s(\xi) = r_{s0}$, Eq. (36) becomes

$$\left[\frac{\partial^3}{\partial \xi \partial \eta^2} - k_g^3(\xi)\right]\delta r = 0, \quad (37)$$

where $k_g^3 = [2k_{p0}/(kr_{s0})]^2 K_G(\xi)$. Equation (37) can be solved taking a Laplace transform in the η variable, yielding

$$\delta r \sim \int_B ds \ \exp\left[s\eta - s^{-2}\int_\xi^0 d\xi' k_g^3\right], \quad (38)$$

where s is the Laplace transform variable and the integration is over the Bromwich contour. The asymptotic behavior of δr can be found by integrating Eq. (38) using the saddle point method,

$$\delta r \sim \exp\left[\frac{3}{4}(1 \pm i\sqrt{3})\left(2\eta^2\int_\xi^0 d\xi' k_g^3\right)^{1/3}\right]. \quad (39)$$

Alternatively, the asymptotic behavior of δr can be determined from Eq. (37) by assuming δr is a function of only the variable $x = (-\xi)^{1/3}\eta^{2/3}$ and assuming k_g^3 is constant. Substituting $\delta r = \delta r(x)$ into Eq. (37) yields

$$\frac{4}{27}(\partial^3/\partial x^3 + \frac{3}{2}x^{-1}\partial^2/\partial x^2 - \frac{1}{2}x^{-2}\partial/\partial x)\delta r = -k_g^3\delta r. \quad (40)$$

In the asymptotic limit, $x \to \infty$, Eq. (40) reduces to

$$(\partial^3/\partial x^3)\delta r = -\frac{27}{4}k_g^3\delta r, \quad (41)$$

which yields the solution in Eq. (39).

The growth rate in Eq. (39) can be simplified by noting that, along the axis $r=0$, the equilibrium plasma density profile is given by $\partial n_p/\partial \xi = -n_{n0}K_G$ and Eq. (39) becomes $\delta r \sim \exp[(1 \pm i\sqrt{3})N_e(\xi,\eta)]$, where

$$N_e = (3/2^{5/3})(n_p/n_{n0})^{1/3}(k_{p0}r_{s0}\eta/Z_{R0})^{2/3} \quad (42)$$

is the number of e folds. If the equilibrium is nearly constant in ξ, the plasma density profile is given by $n_p/n_{n0} = |\xi|K_G$ and the number of e folds is $N_e = \alpha_0|\xi|^{1/3}\eta^{2/3}$ where $\alpha_0 = (3/4)(2K_G)^{1/3}(k_{p0}r_{s0}/Z_{R0})^{2/3}$. The IM instability grows as a function of the distance behind the head of the optical beam, $|\xi|$, and the propagation distance η.

The dependence of N_e on ξ indicates that the number of e folds at the back of the beam is greater than near the front. The IM instability disrupts the back of the beam, and the disruption point propagates toward the front. The disruption point can be defined as the point on the beam where the initial perturbation is increased by $\exp(N_0)$, where $N_0 \gg 1$ is the number of e folds necessary for disruption. This point moves toward the front of the beam with relative velocity $v_d = -c(\partial N_e/\partial \eta)/(\partial N_e/\partial \xi)$, where $N_e(\xi,\eta) = N_0$. For the case where the plasma density profile is linear, i.e., $n_p = K_G n_{n0}|\xi|$, the disruption velocity in the beam frame is

$$v_d = 2cN_0^3\alpha_0^{-3}\eta^{-3}. \quad (43)$$

To gain some understanding of the IM instability, consider increasing the spot size of an initially matched optical beam, i.e., $\delta r(\eta=0) > 0$. In this case the beam intensity and ionization rate are reduced resulting in less plasma generation and enhanced focusing of the beam. The focusing optical beam overshoots its equilibrium value such that $\delta r < 0$ some distance behind the beam front. When $\delta r < 0$, the intensity, ionization rate, and plasma density increase, causing the beam to defocus and overshoot its equilibrium value. This focusing and defocusing of the beam results in the IM instability. The modulation amplitude and period are functions of the distance back from the head of the optical beam, $|\xi|$, and the propagation distance, $\eta = z$, as indicated by Eq. (42).

D. Numerical results for Gaussian beams

1. Dynamic solutions

The propagation dynamics of the fundamental Gaussian beam is studied by numerically solving the envelope equation, Eq. (29), for the spot size $r_s(\xi,\eta)$. The envelope equation is numerically integrated in η (axial propagation distance) using a finite-difference method, where the initial conditions $r_s(\xi,\eta=0)$ and $[\partial r_s(\xi,\eta)/\partial \eta]_{\eta=0}$ are specified. Note that in evaluating the filling factor $\sigma_G(\xi,\eta)$ in Eq. (27), the integral over ξ' is carried out at every η step, since the integrand in Eq. (27) is a function of ξ' and η. We consider a linearly polarized laser pulse with a Gaussian radial profile and an initial ($\eta=z=0$) axial profile given by $E_0(\xi,0) = E_{p0}\sin(\pi|\xi|/L)$ for $-L \leq \xi \leq 0$, where $E_{p0} = (8\pi I_{p0}/c)^{1/2}$ is the initial peak electric field, $I_{p0} = 3.0 \times 10^{13}$ W/cm^2 is the initial peak intensity, and $L = 60$ μm is the pulse length. With wavelength $\lambda = 1$ μm and initial spot size $r_{s0} = 80$ μm, the peak power is $P_0 = 3.0$ GW and the diffraction length is $Z_{R0} = 2.0$ cm. The optical pulse propagates in air at 1 atm: neutral gas density $n_{n0} = 2.7 \times 10^{19}$ cm^{-3}, nonlinear index [37] $n_2 = 5.6 \times 10^{-19}$ cm^2/W, normalized ionization potential $U_I/U_H = 1.07$, and nonlinear focusing power $P_{NG} = 2.8$ GW ($P_0/P_{NG} \simeq 1.1$).

The simulation begins with the optical pulse at focus ($\partial r_s/\partial \eta = 0$) in the neutral gas. With the initial value of the filling factor σ_G computed via Eq. (27), the envelope equation, Eq. (29), is integrated in the simulation variables $\xi = z - vt$ and $\eta = z$. Figures 2(a) and 2(b) show the initial $\eta = 0$ optical beam intensity I and plasma density n_p versus (r,ξ). In Figs. 2(a) and 2(b), the direction of propagation is towards the right. Plots of I and n_p versus radius at the pulse center ($\xi = -30$ μm) are shown in Fig. 2(c) for this case. Note also that the nonlinear nature of the ionization process causes the plasma density gradient versus both r and ξ to be considerably sharper than the intensity gradient.
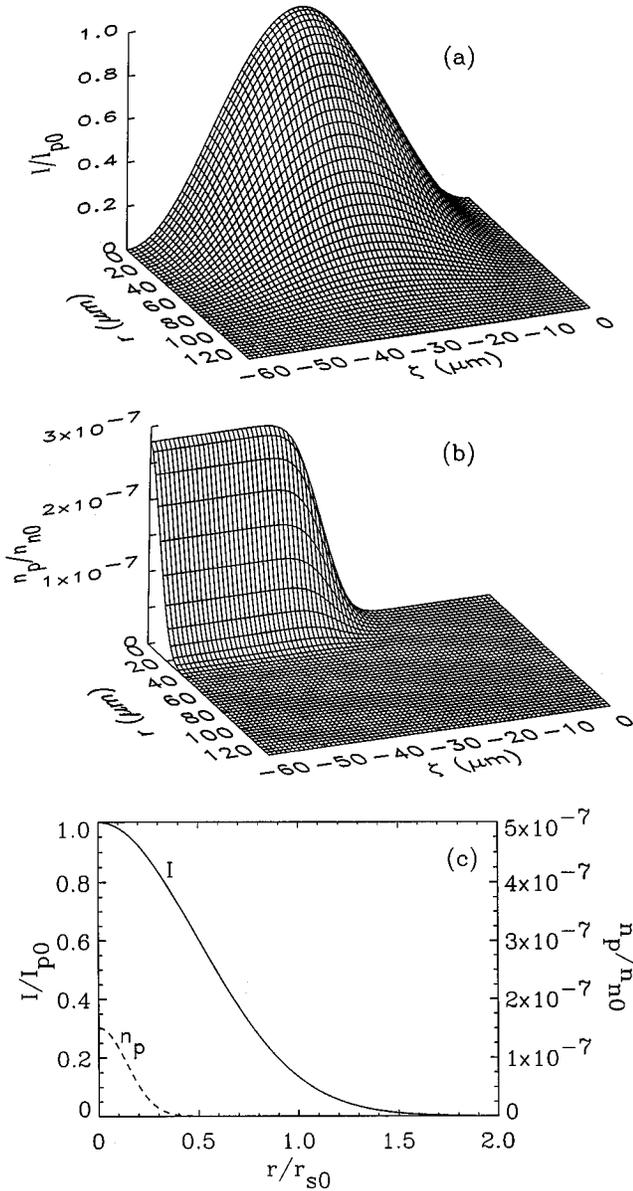
FIG. 2. Surface plots of (a) optical pulse intensity I and (b) plasma density n_p plotted versus (r, ξ) at $\eta = z = 0$ for a fundamental Gaussian beam propagating in air at 1 atm; propagation is towards the right. Plot (c) shows the intensity I (solid line) and plasma density n_p (dashed line) versus r at the pulse center ($\xi = -30$ μm).

The evolution of the optical pulse is shown in Figs. 3(a)–3(d), where the spot size r_s (dashed line), intensity I on axis (solid line), and plasma density n_p on axis (dotted line) are plotted versus ξ at (a) $\eta = z = 0$, (b) 6 cm, (c) 8 cm, and (d) 10 cm. Initially, the spot size is constant along the optical pulse, as shown in Fig. 3(a). Because $P_0 > P_{NG}$, the center of the pulse is focused while the front and back portions diffract, as seen in Fig. 3(b). At $\xi \simeq -25$ μm, where $P \simeq P_{NG}$ and $n_p \ll n_{n0}$, diffraction balances nonlinear focusing and the spot size remains constant at $r_s = r_{s0}$. Behind this point, focusing increases the optical intensity, producing a corresponding increase in the ionization rate. Because ionization is a highly nonlinear process, the steepness of the plasma density gradient also increases. Increased ionization and increased plasma density gradients are shown in Figs. 3(b)–3(d). Increased

ionization causes the latter portion of the optical pulse to diffract, as can be seen in Figs. 3(c) and 3(d). The rapid change in the plasma density at the steepening ionization front results in a correspondingly rapid change in the focusing of the optical pulse. This results in an increasingly narrow intensity spike at the ionization front.

The optical pulse structure observed in Figs. 3(c) and 3(d) occurs even when the power P greatly exceeds the nonlinear focusing threshold P_{NG}. For example, Figs. 4(a)–4(d) show the evolution of a pulse with $P_0/P_{NG} = 2$. Except for the initial power and the initial spot size $r_{s0} = 110$ μm (and a corresponding change in $Z_{R0} = 3.8$ cm), the parameters of Fig. 4 are identical to those of Fig. 3. As in Fig. 3, there is a point near the front of the pulse in Fig. 4 (at $\xi \simeq -15$ μm) where $P \simeq P_{NG}$, $n_p \ll n_{n0}$, and diffraction balances nonlinear focusing. Also as before, nonlinear focusing of the pulse behind this point leads to an increasingly steep ionization front. This, in turn, produces an increasingly narrow optical intensity spike.

2. Self-guided solutions

Examples of matched beam equilibria are shown in Figs. 5 and 6. In both cases, we consider a linearly polarized $\lambda = 1$ μm optical pulse with a Gaussian radial profile propagating in air at 1 atm ($n_{n0} = 2.7 \times 10^{19}$ cm^{-3}, $n_2 = 5.6 \times 10^{19}$ cm^2/W, $U_I/U_H = 1.07$, and $P_{NG} = 2.8$ GW). Figure 5 shows optical power profiles (solid lines) and plasma density profiles (dashed lines) plotted versus ξ along the axis for equilibria with constant $E_0(\xi)$ profiles. Equilibria are shown for three different values of the optical intensity: $I_p = I_1 = 5 \times 10^{13}$ W/cm^2, $I_2 = 6 \times 10^{13}$ W/cm^2, and $I_3 = 7 \times 10^{13}$ W/cm^2. Here, $E_0(\xi) = (8\pi I_p/c)^{1/2}$ is constant along the length of the optical pulse, such that the variation in power $P(\xi)$ corresponds to a variation in spot size $r_s = (2P/\pi I_p)^{1/2}$. Note that the constant E_0 profile produces a constant ionization rate and a linear rise in $n_p/n_{n0} \ll 1$. Also, the power profiles are exponential functions as given in Eq. (35).

Figure 6 shows optical power and plasma density profiles for equilibria with constant $r_s(\xi) = r_{s0}$ profiles. In this case, matched $E_0(\xi)$ profiles are determined numerically from Eq. (34) for three different values of the leading-edge ($\xi = 0$) intensity: $I_p = I_1 = 5 \times 10^{13}$ W/cm^2, $I_2 = 5.1 \times 10^{13}$ W/cm^2, and $I_3 = 5.2 \times 10^{13}$ W/cm^2. In this case, the variation in optical power $P(\xi)$ corresponds to a variation in intensity $I_p = 2P/\pi r_{s0}^2$, such that E_0 increases with $|\xi|$ along the length of the pulse. As a result, the ionization rate increases as a function of $|\xi|$. Increased ionization (defocusing) requires increased power (focusing) to compensate, further increasing the ionization in a highly nonlinear manner. As a result, the constant-r_s equilibrium profiles can be very sensitive to the value of I_p as in Fig. 6.

3. Ionization-modulation instability

An example of the IM instability for a fundamental Gaussian beam obtained by numerical solution of the envelope equation, Eq. (29), is shown in Fig. 7. Here, we consider the propagation in air of a constant-r_s equilibrium with $I_p(\xi = 0) = 3.0 \times 10^{13}$ W/cm^2, $r_s = r_{s0} \simeq 78$ μm, and $Z_{R0} \simeq 1.9$ cm. In this case, there is very little initial ionization and the growth of the instability is extremely slow with $P(\xi)$
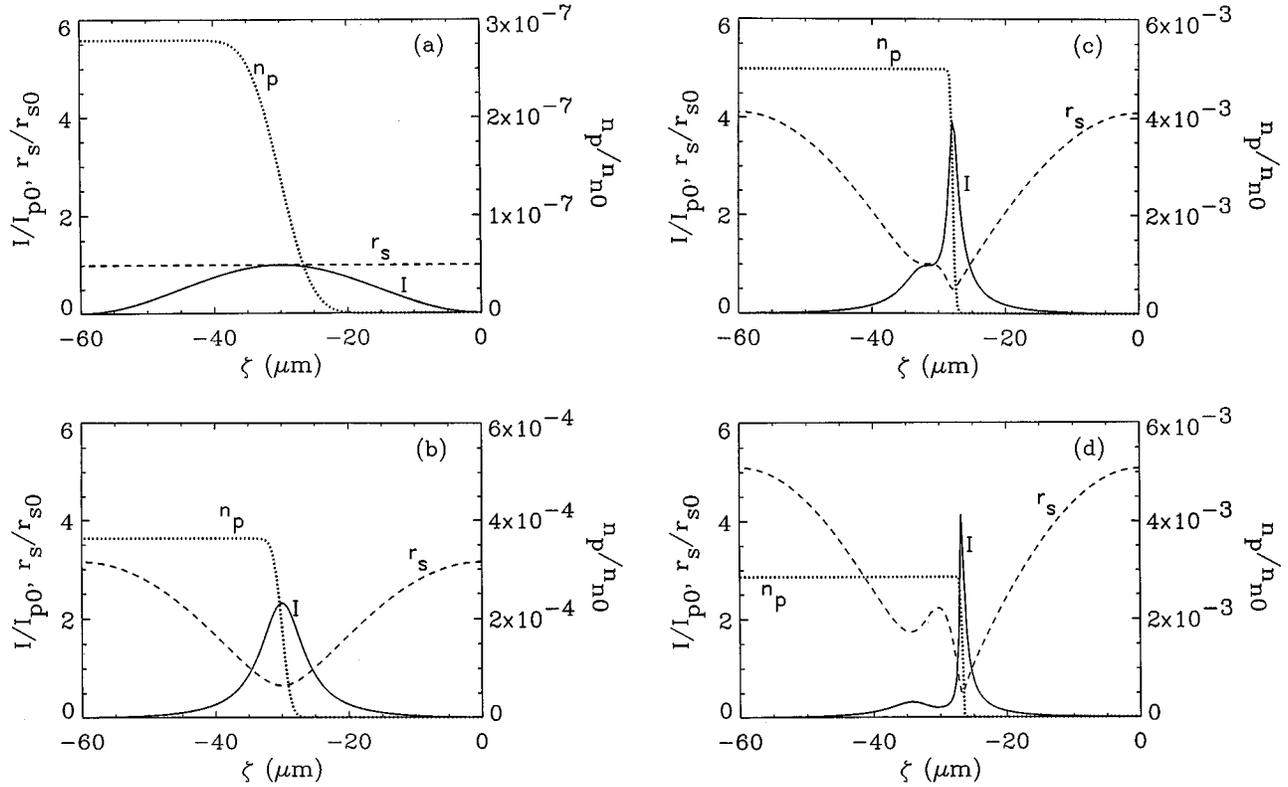
FIG. 3. Spot size r_s (dashed line), intensity I (solid line), and plasma density n_p (dotted line) plotted versus ξ on axis at (a) $\eta=z=0$, (b) 6 cm, (c) 8 cm, and (d) 10 cm. The initial peak intensity is $I_{p0}=3.0\times10^{13}$ W/cm^2, the initial spot size is $r_{s0}=80$ μm, and the peak power is $P_0=3.0$ GW$\simeq1.1P_{NG}$. The direction of propagation is towards the right.
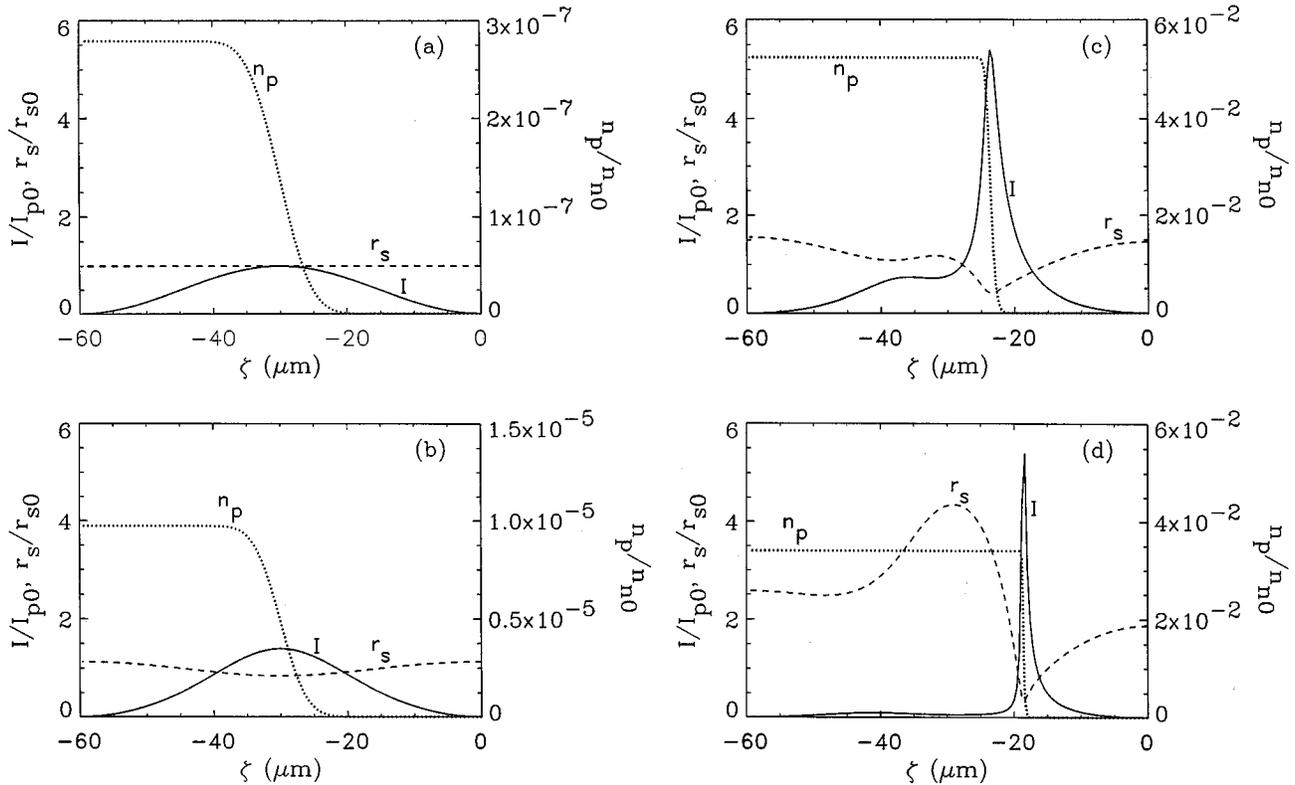
FIG. 4. Spot size r_s (dashed line), intensity I (solid line), and plasma density n_p (dotted line) plotted versus ξ on axis at (a) $\eta=z=0$, (b) 6 cm, (c) 8 cm, and (d) 10 cm. Here, $I_{p0}=3.0\times10^{13}$ W/cm^2, $r_{s0}=110$ μm, and $P_0=5.6$ GW$\simeq2.0P_{NG}$.
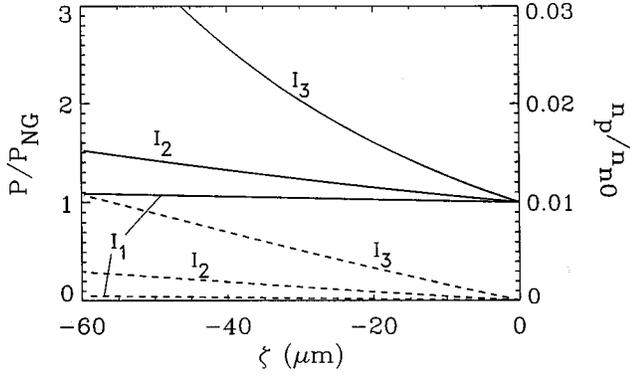
FIG. 5. Equilibrium profiles of power P (solid lines) and plasma density on axis n_p (dashed lines) plotted versus ξ for three different values of intensity I_p: $I_1 = 5 \times 10^{13}$ W/cm^2, $I_2 = 6 \times 10^{13}$ W/cm^2, and $I_3 = 7 \times 10^{13}$ W/cm^2. Here, $E_0 = (8\pi I_p/c)^{1/2}$ is constant versus ξ such that $r_s = (2P/\pi I_p)^{1/2}$.

$\simeq P_{NG} = 2.8$ GW along the length of the optical pulse. The evolution of the optical pulse is shown in Figs. 7(a)–7(f), where the spot size r_s (solid line) and plasma density n_p on axis (dashed line) are plotted versus ξ at (a) $\eta = z = 0$, (b) 400 cm, (c) 450 cm, (d) 500 cm, (e) 550 cm, and (f) 600 cm. In Fig. 7, the direction of propagation is towards the right.

The simulation begins, Fig. 7(a), with the optical pulse at focus ($\partial r_s/\partial \eta = 0$) in the neutral gas. In Fig. 7(a), the spot size r_s is constant along the pulse and $n_p(\xi)$ increases linearly since E_0 is approximately constant. At later times, Figs. 7(b)–7(d), oscillations in r_s cause oscillations in the ionization rate such that each region where r_s has decreased corresponds to an increase in ionization. This is particularly noticeable at the back of the pulse ($\xi = -60$ μm) is Fig. 7(c).

Eventually, there is a large enough increase in the plasma density so that the latter portion of the optical pulse is defocused, i.e., the guiding is disrupted. When the optical pulse is sufficiently defocused the ionization rate falls and $dn_p/d\xi \simeq 0$. Thus, an ''ionization front'' develops which propagates forward in the beam frame. This can be seen in Fig. 7(e), where the ionization front is at $\xi \simeq -40$ μm, and in Fig. 7(f), where the ionization front is at $\xi \simeq -33$ μm. Fig-
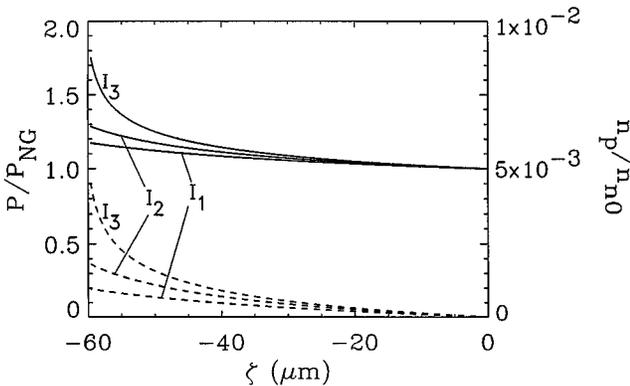
FIG. 6. Equilibrium profiles of power P (solid lines) and plasma density n_p on axis (dashed lines) plotted versus ξ for three different values of leading-edge ($\xi = 0$) intensity $I_p = I_1 = 5.0 \times 10^{13}$ W/cm^2, $I_2 = 5.1 \times 10^{13}$ W/cm^2, and $I_3 = 5.2 \times 10^{13}$ W/cm^2. Here, r_s is constant versus ξ such that $I(\xi) = 2P(\xi)/\pi r_{s0}^2$.

ures 7 indicate that the disruption velocity is in good agreement with Eq. (43).

The growth of the instability of Fig. 7 is plotted versus ξ at fixed $\eta = z = 550$ cm in Fig. 8(a), where $\ln|\Delta r|$, from the numerical integration of the envelope equation, is compared to the number of e folds N_e from Eq. (42). Here, $\Delta r = (r_s - r_{s0})/r_{s0}$. Similarly, $\ln|\Delta r|$ versus $\eta = z$ at fixed $\xi = -49$ μm is shown in Fig. 8(b). For both plots, excellent agreement is observed between the slope of $N_e(\xi)$ and the peaks of the $\ln|\Delta r|$ curve. As expected, agreement tends to break down for ξ, $\eta \to 0$, where the growth is not yet asymptotic, and for $\ln|\Delta r| \to 0$, where the growth is nonlinear.

IV. HIGHER-ORDER RADIALLY POLARIZED BEAM PROPAGATION

We now consider the dynamics of a radially polarized optical beam propagating in a gas undergoing ionization. The radially polarized optical beam is formed by taking $m = 0$, $p = 1$ in Eq. (14), setting $a_{0,1} = b_{0,1} = E_0 \exp(i\theta_0)$, $\hat{\mathbf{e}}_\perp = \hat{\mathbf{e}}_x$ and $\hat{\mathbf{e}}_\perp' = \hat{\mathbf{e}}_y$. The resulting field, from Eqs. (6) and (14), is

$$\mathbf{E} \simeq E_0(\sqrt{2}r/r_s)\exp(-r^2/r_s^2 + i\psi)\hat{\mathbf{e}}_r/2 + \text{c.c.}, \qquad (44)$$

where $\psi = k\xi + \theta_0 + \alpha r^2/r_s^2$ and $\hat{\mathbf{e}}_r = (\cos\theta)\hat{\mathbf{e}}_x + (\sin\theta)\hat{\mathbf{e}}_y$ is the unit radial vector. The functions E_0, θ_0, α, and r_s satisfy Eqs. (21) and (22) with $p = 1$. From Eq. (22a), $E_0(\xi, \eta) = E_0(\xi, \eta = 0)r_s(\xi, \eta = 0)/r_s(\xi, \eta)$, where $E_0^2(\xi, \eta = 0)r_s^2(\xi, \eta = 0)$ is proportional to the optical beam power $P(\xi)$. The axial field component associated with the radial field in Eq. (44), as obtained from $\boldsymbol{\nabla} \cdot \mathbf{E} = 0$, is maximum along the axis and given by

$$\mathbf{E}_z \simeq \frac{2\sqrt{2}i}{kr_s} E_0[1 - (r^2/r_s^2)(1 - i\alpha)]\exp(-r^2/r_s^2 + i\psi)\hat{\mathbf{e}}_z/2$$
$$+ \text{c.c.}, \qquad (45a)$$

$$\mathbf{E}_z(r=0) \simeq \frac{2\sqrt{2}i}{kr_s} E_0 \exp(ik\xi + i\theta_0)\hat{\mathbf{e}}_z/2 + \text{c.c.}, \quad (45b)$$

where the expression in Eq. (45b) is valid along the z axis, i.e., $r = 0$. The intensity and power associated with the radially polarized beam in a medium of refractive index n_0 are, respectively,

$$I = (c/4\pi)\langle \mathbf{E} \times \mathbf{B} \rangle \cdot \hat{\mathbf{e}}_z = I_p \chi \exp(1 - \chi), \qquad (46a)$$

$$P = (\pi/2)r_s^2 \int_0^\infty d\chi\, I(\chi) = (e\pi/2)r_s^2 I_p, \qquad (46b)$$

where $I_p = (cn_0/8\pi)E_0^2/e$ is the maximum intensity, which occurs at $\chi = 1$ ($r = r_s/\sqrt{2}$), $e \simeq 2.72$ and $\langle\ \rangle$ denotes time averaging. Similar higher-order radially polarized modes have been produced using an axicon focusing configuration [38,39].

To determine the optical beam dynamics from Eqs. (21) and (22) the source functions $G(\eta)$ and $H(\eta)$ in Eq. (20) are evaluated with $p = 1$. Substituting K^2 from Eq. (13) into Eq. (20) and integrating over η yields
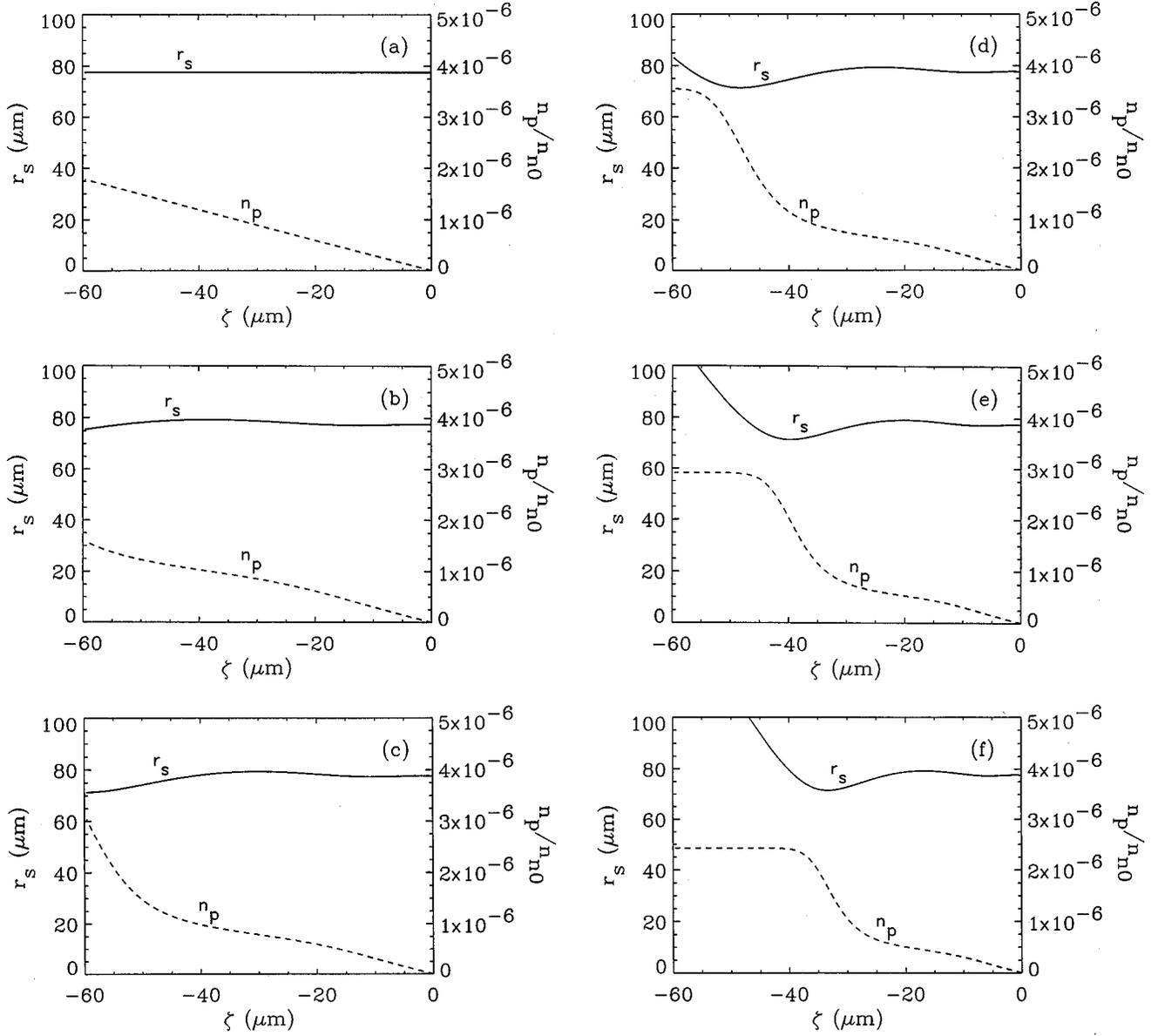
FIG. 7. Spot size r_s (solid line) and plasma density n_p on axis (dashed line) plotted versus ξ at (a) $\eta = z = 0$, (b) 400 cm, (c) 450 cm, (d) 500 cm, (e) 550 cm, and (f) 600 cm, for an initially matched laser pulse with $I_p = 3.0 \times 10^{13}$ W/cm^2 and $r_s(\xi) \simeq 78$ μm propagating in air. The direction of propagation is towards the right.

$$\left.\begin{matrix} G \\ H \end{matrix}\right\} = -(k/2)\left[(e/2)(n_2/n_0)I_p\left\{\begin{matrix} 1 \\ 1/4 \end{matrix}\right\} + (k_{p0}/k)^2\left\{\begin{matrix} \sigma_{R1} \\ \sigma_{R2} \end{matrix}\right\}\right], \quad (47)$$

where the filling factors $\sigma_{R1,2}$ are given by

$$\left.\begin{matrix} \sigma_{R1} \\ \sigma_{R2} \end{matrix}\right\} = \int_0^\infty d\chi (k_p/k_{p0})^2 \chi e^{-\chi}\left\{\begin{matrix} 1 \\ 1 - \chi/2 \end{matrix}\right. . \quad (48)$$

The tunneling ionization rate $W(|\hat{\mathbf{E}}|)$ is maximum when the optical field is maximum. The magnitude of the radial polarized field in the expression for k_p^2, Eq. (12), can be written as $|\hat{\mathbf{E}}| = E_0(1 + y)^{1/2}\exp[(1 + y)/2]$, where $y = 2r^2/r_s^2(\xi') - 1$, and has a maximum at $y = 0$, i.e., $r = r_s(\xi')/\sqrt{2}$. Expanding $|\hat{\mathbf{E}}|$ for $y \ll 1$ gives $|\hat{\mathbf{E}}| \simeq (E_0/\sqrt{e})(1 - y^2/4)$. Using this expression in $W(|\hat{\mathbf{E}}|)$, and noting that $W(|\hat{\mathbf{E}}|)$ is highly peaked about $y = 0$, gives

$$k_p^2(\xi)/k_{p0}^2 \simeq e\int_\xi^0 d\xi' K_R(\xi')e^{-b_R(\xi')y^2/4}, \quad (49)$$

where

$$K_R(\xi) = 4n_0(3/\pi)^{1/2}e^{-3/4}(\Omega_0/c)(\widetilde{U}_I)^{7/4}[\widetilde{E}_0(\xi)]^{-1/2}$$
$$\times \exp[-b_R(\xi)], \quad (50a)$$

$$b_R(\xi) = \tfrac{2}{3}e^{1/2}(\widetilde{U}_I)^{3/2}/\widetilde{E}_0(\xi), \quad (50b)$$

and $\widetilde{E}_0 = E_0/E_H$. Inserting Eq. (49) into the expressions for the filling factors, Eq. (48), and assuming $b_R \gg 1$ allows the integration over r to be carried out yielding
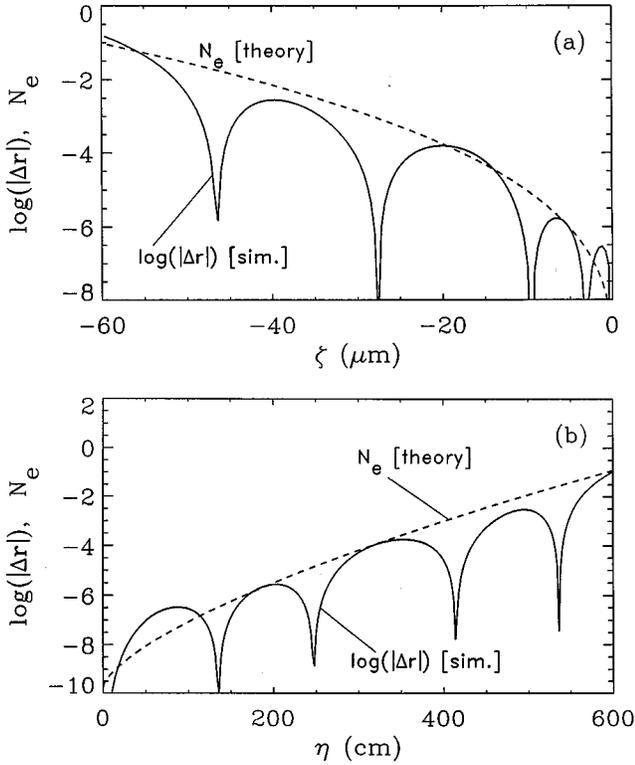
FIG. 8. Perturbed radius $\ln|\Delta r|$ (solid line) and number of e folds N_e (dashed line) plotted (a) versus ξ at fixed $\eta = 550$ cm and (b) versus η at fixed $\xi = -49$ μm. Here, $\Delta r = (r_s - r_{s0})/r_{s0}$ is determined from the integration of the envelope equation, Eq. (29), while N_e is given by Eq. (42). Note that log is the natural logarithm to base e, i.e., ln.

$$\left.\begin{matrix}\sigma_{R1}\\\sigma_{R2}\end{matrix}\right\} = 2\sqrt{\pi}\int_{\xi}^{0}d\xi' K_R(\xi')b_R^{-1/2}(\xi')\left\{\begin{matrix}1\\1-X_s^2/2\end{matrix}\right\}X_s^4$$

$$\times \exp(1-X_s^2), \qquad (51)$$

where $X_s = r_s(\xi')/r_s(\xi)$.

A. Envelope equation for the higher-order beam

Using Eq. (47) for the source function H, the envelope equation in Eq. (21) becomes

$$\partial^2 R/\partial \eta^2 = Z_{R0}^{-2}R^{-3}(1 - P/P_{NR} + \tfrac{1}{2}r_s^2 k_{p0}^2 \sigma_{R2}), \qquad (52)$$

where r_{s0} is constant, $Z_{R0} = kr_{s0}^2/2 = \pi n_0 r_{s0}^2/\lambda$ is the Rayleigh length associated with the spot size r_{s0}, $R = r_s/r_{s0}$ is the normalized spot size, $P = (e\pi/2)I_p r_s^2$ is the total power, and $P_{NR} = 4P_{NG} = 2\lambda^2/(\pi n_0 n_2)$ is the nonlinear focusing power for the higher-order radially polarized beam. The terms on the right-hand side of Eq. (52) denote, respectively, vacuum diffraction, nonlinear focusing, and plasma defocusing. In the absence of ionization, $\sigma_{R2} = 0$, the solution to Eq. (52) for r_s is given by Eq. (30) with P_{NG} replaced by P_{NR}.

B. Self-guided higher-order beam

The condition for a matched beam, i.e., $\partial^2 R/\partial \eta^2 = 0$, is given by

$$P/P_{NR} - 1 = k_{p0}^2 r_s^2 \sigma_{R2}/2 \geqslant 0. \qquad (53)$$

Equation (53) describes a family of equilibrium solutions, i.e., there are various equilibrium profiles $P(\xi)$, $E_0(\xi)$, and $r_s(\xi)$ which satisfy Eq. (53). For the special case of a constant spot size matched beam, $r_s = r_{s0}$, the matched-beam power is given by

$$\partial P/\partial \xi = -(\sqrt{\pi}/2)k_{p0}^2 P_{NR} r_{s0}^2 K_R(\xi)/b_R^{1/2}(\xi), \qquad (54)$$

where $K_R(\xi)$ and $b_R(\xi)$ are functions of $P(\xi)$ through $E_0(\xi)$, i.e., $P(\xi) = (cn_0/16)E_0^2(\xi)r_{s0}^2$.

C. Stability of the higher-order beam

The stability of the matched-beam equilibrium can be analyzed by perturbing the envelope equation, Eq. (52), about the matched-beam solution. This is accomplished by introducing a constant power perturbation to the spot size and field amplitude of the form $r_s(\xi) + \delta r(\xi, \eta)$ and $E_0(\xi) + \delta E(\xi, \eta)$, where $\delta E/E_0 = -\delta r/r_s$. In the limit $b_R \gg 1$, the envelope perturbation satisfies the equation

$$\partial^2 \delta r/\partial \eta^2 = -\frac{\sqrt{\pi}}{2}\frac{k_{p0}^2 r_{s0}}{Z_{R0}^2 R^3}\int_{\xi}^{0}d\xi'[(2-X_s^2)b_R(\xi')\delta r(\xi')$$

$$+ 2X_s(2-4X_s^2+X_s^4)\delta r(\xi)]$$

$$\times r_s(\xi')K_R(\xi')b_R^{-1/2}(\xi')X_s^2 e^{1-X_s^2}. \qquad (55)$$

For a constant spot size equilibrium, $X_s = 1$, Eq. (55) becomes

$$\left(\frac{\partial^2}{\partial \eta^2} - 2\int_{\xi}^{0}d\xi'\frac{k_r^3}{b_R}\right)\frac{\partial \delta r}{\partial \xi} = k_r^3(\xi)\delta r, \qquad (56)$$

where $k_r^3 = 2\sqrt{\pi}[k_{p0}/(kr_{s0})]^2 K_R b_R^{1/2}$. In the limit $b_R \gg N_e \gg 1$, where N_e is the number of e folds of the instability, the second term on the left of Eq. (56) can be neglected and the asymptotic behavior of δr is given by

$$\delta r \sim \exp\left[\frac{3}{4}(1\pm i\sqrt{3})\left(2\eta^2\int_{\xi}^{0}d\xi' k_r^3\right)^{1/3}\right]. \qquad (57)$$

Notice that, for an equilibrium in which $E_0(\xi)$ is nearly constant, the peak equilibrium plasma density occurs at $r = r_s/\sqrt{2}$ and is given by $n_p/n_{n0} \simeq -eK_R\xi$. In this limit, the asymptotic behavior of δr can be written as $\delta r \sim \exp[(1\pm i\sqrt{3})N_e]$, where

$$N_e = \frac{3}{4}\left(\frac{\sqrt{\pi}}{e}b_R^{1/2}(n_p/n_{n0})(k_{p0}r_{s0}\eta/Z_{R0})^2\right)^{1/3}, \qquad (58)$$

is the number of e folds. Hence, the growth rate of the IM instability for the higher-order optical beam differs roughly by a factor of $(\pi b_R/4e^2)^{1/6} \sim 1$ from that of the fundamental, assuming equal values at $k_{p0}r_{s0}$, n_p/n_{n0}, and η/Z_{R0}.

D. Numerical results for the higher-order beam

1. Dynamic solutions

The propagation dynamics of a higher-order radially polarized laser pulse can be described by a numerical solution of the envelope equation, Eq. (52). Initially, $\eta = z = 0$, the
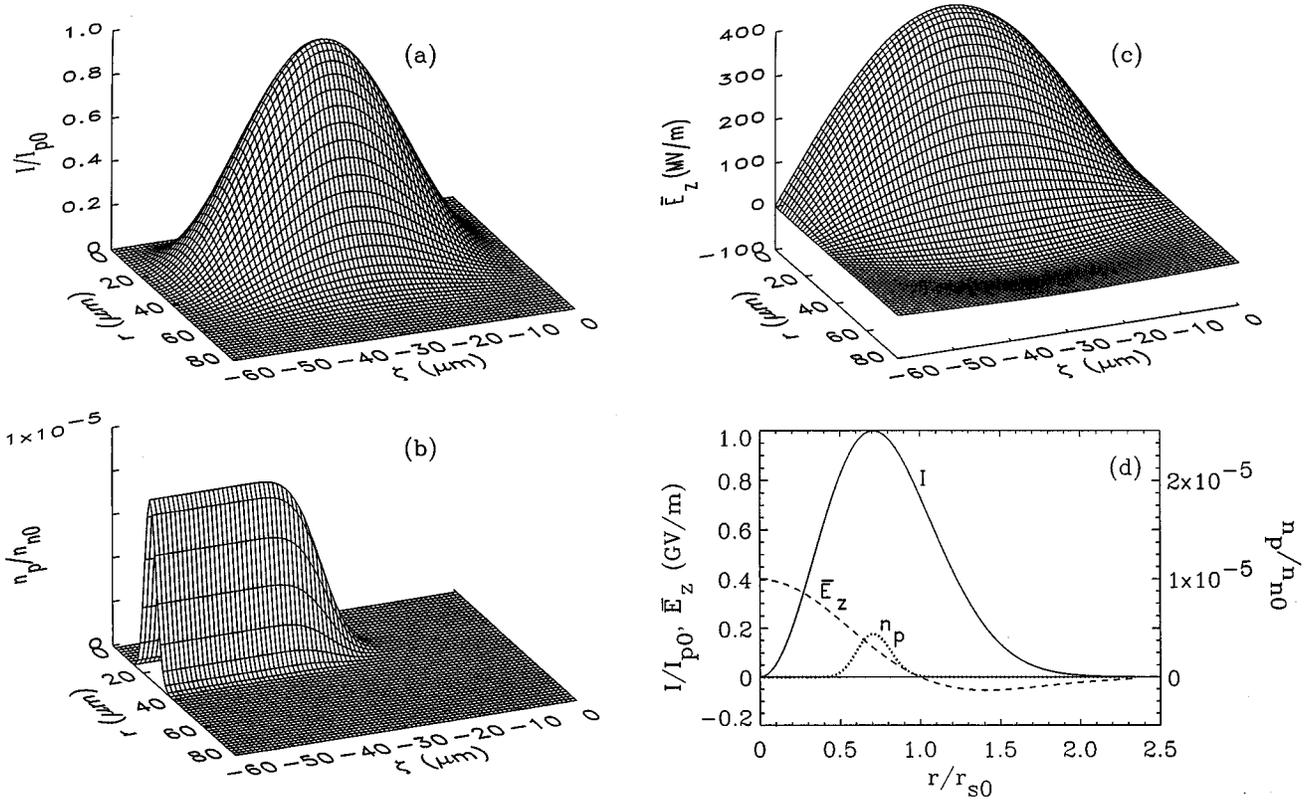
FIG. 9. Surface plots of (a) optical pulse intensity, I, (b) plasma density n_p, and (c) accelerating field $\bar{E}_z = |\hat{E}_z|$ plotted versus (r, ξ) at $\eta = z = 0$ for a higher-order radially polarized beam propagating in H_2 at 30 atm. The direction of propagation is towards the right. Plot (d) shows the intensity (solid line), accelerating field $\bar{E}_z$ (dashed line), and plasma density n_p (dotted line) plotted versus r at the pulse center.

profile of the radial electric field is $|E(r,\xi)| = E_0(\xi,0)(\sqrt{2}r/r_s)\exp(-r^2/r_s^2)$, with an axial profile $E_0(\xi,0) = E_{p0}e^{1/2}\sin(\pi|\xi|/L)$ for $-L \leq \xi \leq 0$, where $L = 60$ μm is the optical pulse length. The peak initial field, occurring at $r = r_s/\sqrt{2}$, is $E_{p0} = (8\pi I_{p0}/c)^{1/2}$, where $I_{p0} = 4.7 \times 10^{13}$ W/cm^2 is the peak initial optical intensity. With wavelength $\lambda = 1$ μm and initial spot size $r_{s0} = 35$ μm, the peak power is $P_0 = 2.5$ GW and the diffraction length is $Z_{R0} = 0.4$ cm. We consider propagation in hydrogen (H_2) at 30 atm: nonlinear index [4] $n_2 = 3.3 \times 10^{-18}$ cm^2/W, ionization energy $U_I = 15.4$ eV, neutral density $n_{n0} = 8.1 \times 10^{20}$ cm^{-3}, and nonlinear focusing power $P_{NR} = 1.9$ GW ($P_0/P_{NR} \approx 1.3$). Hydrogen is chosen for its low atomic number Z_a and, hence, Bremsstrahlung losses can be neglected, see Appendix C.

The simulation begins with the optical pulse at focus $(\partial r_s/\partial \eta = 0)$ in the neutral gas with intensity $I(r,\xi)$ and plasma density $n_p(r,\xi)$ profiles initialized as shown in Figs. 9(a) and 9(b), where the direction of propagation is towards the right. The accelerating field $\bar{E}_z = |\hat{E}_z|$ profile is plotted in Fig. 9(c), where $E_z = \hat{E}_z\exp(ik\xi)/2 + \text{c.c.}$ with E_z given by Eq. (45). Plots of I, $\bar{E}_z$, and n_p versus radius at the pulse center ($\xi = -30$ μm) are shown in Fig. 9(d) for this case. The highly nonlinear nature of the ionization process causes the plasma density gradient versus both r and ξ to be considerably sharper than the intensity gradient.

The evolution of the optical pulse is shown in Figs. 10(a)–10(d), where the spot size r_s (dashed line), accelerating field $\bar{E}_z$ on axis (solid line), and plasma density n_p (dotted line) are plotted versus ξ at (a) $\eta = z = 0$, (b) 0.4 cm, (c) 0.7 cm, and (d) 1.0 cm. In Figs. 10(a)–10(d), $n_p(\xi)$ is evalu-

ated at $r = r_{\min}/\sqrt{2}$, where $r_{\min}$ is the minimum value of $r_s(\xi)$. Initially, the spot size is constant along the optical pulse, and the peak accelerating field is $\bar{E}_z \simeq 400$ MV/m, as in Fig. 10(a). Since $P_0 > P_{NR}$, the center of the pulse is focused while the front and back portions diffract, as shown in Fig. 10(b). The increasing optical intensity in the center of the pulse increases the accelerating field since $\bar{E}_z \sim I^{1/2}$. Diffraction balances nonlinear focusing at $\xi \simeq -21$ μm, where $P \simeq P_{NR}$, and the spot size remains constant, $r_s = r_{s0}$. Behind this point, focusing increases the optical intensity, producing a corresponding increase in the ionization rate. Increased ionization and increased plasma density gradients are shown in Figs. 10(a)–10(c). Increased ionization causes the optical pulse to diffract, reducing $\bar{E}_z$ in the latter portion of the pulse, as shown in Figs. 10(c) and 10(d). The rapid change in the plasma density at the steepening ionization front results in a corresponding rapid change in the focusing of the pulse. This results in an increasingly narrow spike in $\bar{E}_z$ at the ionization front. The peak accelerating field is $\bar{E}_z \simeq 1.1$ GV/m at $\eta = z = 1.0$ cm $\simeq 2.5 Z_{R0}$.

2. Self-guided solutions

An example of a self-guided, higher-order radially polarized beam of wavelength $\lambda = 1$ μm propagating in hydrogen (H_2) at 30 atm is shown in Fig. 11. For H_2 at 30 atm, $n_{n0} = 8.1 \times 10^{20}$ cm^{-3}, $n_2 = 3.3 \times 10^{-18}$ cm^2/W, $U_I/U_H = 1.1$, and $P_{NR} \simeq 1.9$ GW. The matched beam conditions can be determined from Eq. (53) together with Eq. (51) for a given axial intensity profile. For equilibria with constant $E_0(\xi)$ pro-
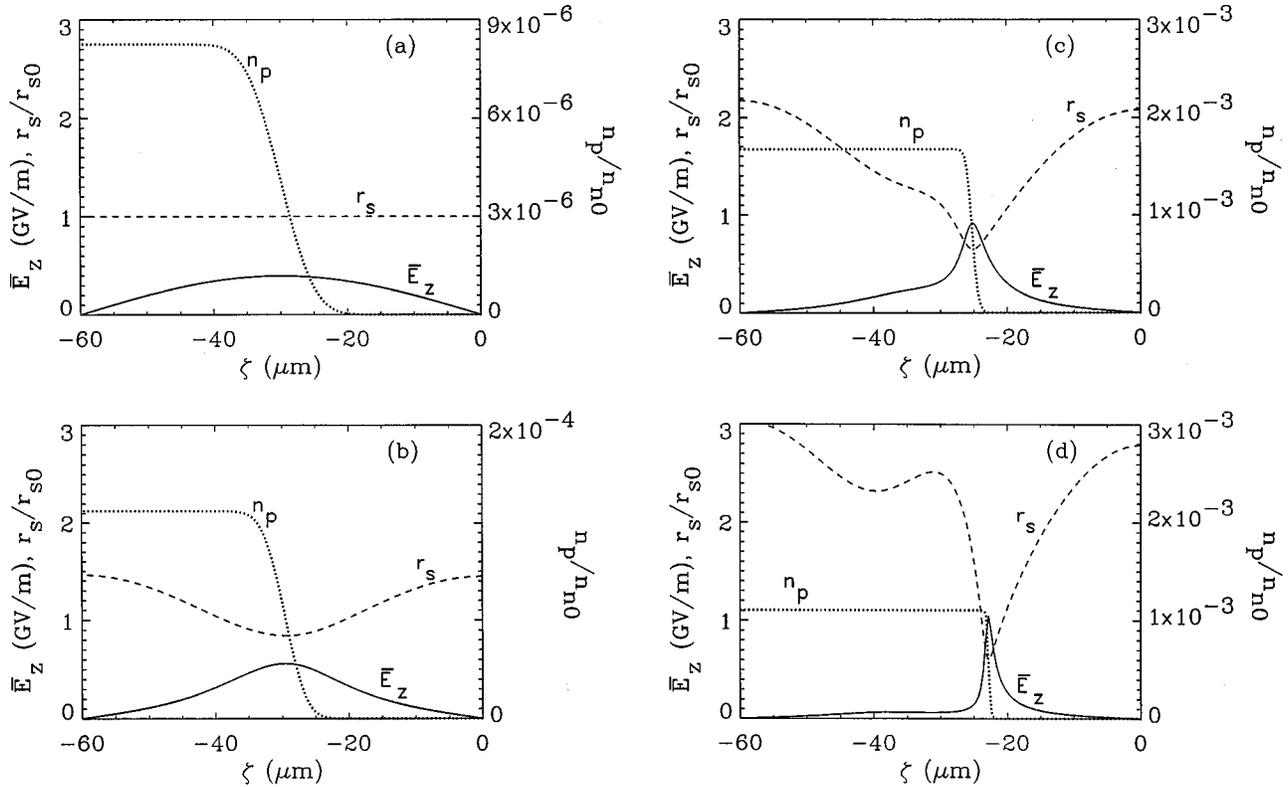
FIG. 10. Spot size r_s (dashed line), accelerating field $\bar{E}_z$ on axis (solid line), and plasma density n_p at $r=r_{min}/\sqrt{2}$ (dotted line) plotted versus ξ at (a) $\eta=z=0$, (b) 0.4 cm, (c) 0.7 cm, and (d) and 1.0 cm. Here, the initial spot size is $r_{s0}=35$ μm, the peak power is $P_0=2.5$ GW $\simeq 1.3 P_{NR}$, and the direction of propagation is towards the right.

files, i.e., constant peak intensity of $I_p=4.7\times10^{13}$ W/cm^2, the matched profiles for power P and plasma density n_p at $r=r_{min}/\sqrt{2}$ versus ξ are shown in Fig. 11. For these parameters, the degree of ionization is small, $n_p/n_{n0}\leq10^{-4}$. The spot size is given by $r_s^2(\xi)=2P(\xi)/(\pi e I_p)$, which gives $r_s(\xi=0)=r_{min}=31$ μm at the front of the beam. The on-axis accelerating field, also shown in Fig. 11, has the maximum value 450 MV/m at the front of the optical beam. Since $\bar{E}_z\sim n_2^{1/2}\sim n_{n0}^{1/2}$, the accelerating gradient can be increased by increasing the gas pressure.
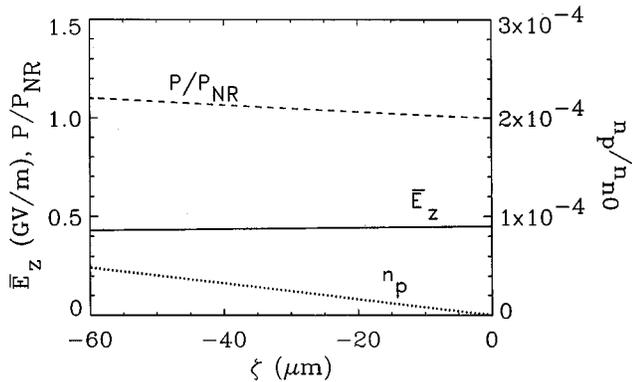
3. Ionization-modulation instability

As discussed in Sec. IV C, the optical beam undergoes an IM instability. Numerical simulations of Eq. (52) show that, with a 1% initial perturbation of the spot size, the IM instability significantly disrupts the equilibrium beam profile of Fig. 11 after $\sim$10 cm of propagation. The growth rate of the IM instability is a highly nonlinear function of the optical intensity through the plasma density. Reducing the intensity in the example of Fig. 11 to 3.2×10^{13} W/cm^2 (which reduces $\bar{E}_z$ to 300 MeV/m) results in a matched beam with very little ionization (the plasma density is reduced by a factor of $\sim$130) and little variation in power and spot size along the length of the optical pulse. Simulations show that with a 1% perturbation in the spot size, the pulse propagates >1 m without significant disruption. The behavior of the IM instability is shown in the following numerical example. In this example, however, the instability is allowed to grow from numerical noise to facilitate comparison to the theoretical growth rate.

Propagation of a guided pulse in H$_2$ at 30 atm is shown in Fig. 12. Initially, $I_p=3.2\times10^{13}$ W/cm^2 is constant throughout the pulse, the peak accelerating field is $\bar{E}_z=300$ MV/m, the spot size is $r_s\simeq37$ μm ($Z_{R0}\simeq0.44$ cm), and $P(\xi)\simeq P_{NR}=1.9$ GW. The evolution of the optical pulse is shown in Figs. 12(a)–12(d), where the spot size r_s (dashed line), accelerating field $\bar{E}_z$ on axis (solid line), and plasma density n_p at $r=r_{min}/\sqrt{2}$ (dotted line) are plotted versus ξ at (a) $\eta=z=0$, (b) 60 cm, (c) 75 cm, and (d) 90 cm. Initially, the spot size is constant along the optical pulse, and the peak

FIG. 11. Accelerating field $\bar{E}_z$ on axis (solid line), power P (dashed line) and plasma density n_p at $r=r_{min}/\sqrt{2}$ (dotted line) plotted versus ξ for intensity $I_p=4.7\times10^{13}$ W/cm^2. Here, E_0 is constant versus ξ.
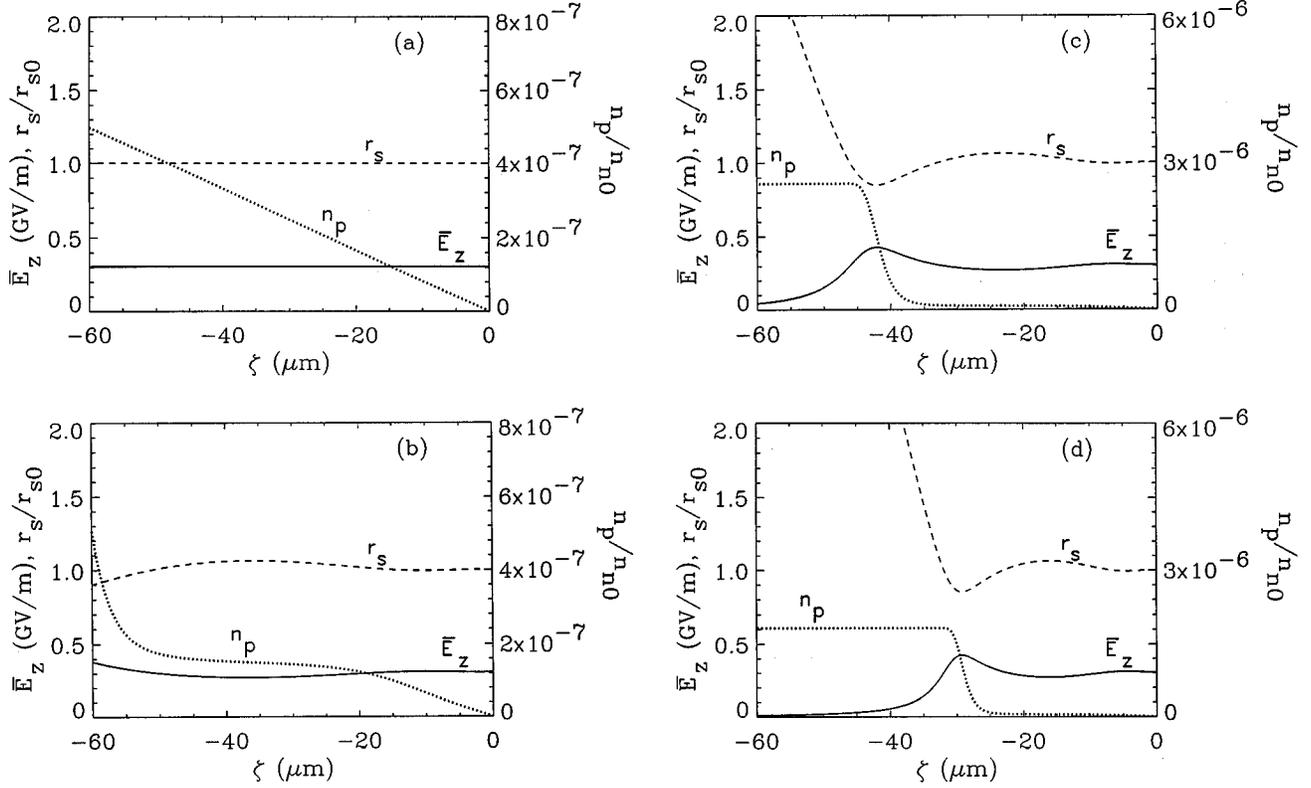
FIG. 12. Accelerating field $\bar{E}_z$ on axis (solid line), spot size r_s (dashed line), and plasma density n_p at $r = r_{\min}/\sqrt{2}$ (dotted line) plotted versus ξ at (a) $\eta = z = 0$, (b) 60 cm, (c) 75 cm, and (d) and 90 cm, for an initially matched optical pulse with $I_p = 3.2 \times 10^{13}$ W/cm^2 propagating in H$_2$ at 30 atm. This initial radius is $r_s(\xi) \simeq 37$ μm. The direction of propagation is towards the right.

accelerating field is $\bar{E}_z \simeq 300$ MV/m, as in Fig. 12(a). At later times, Figs. 12(b)–12(d), oscillations in r_s cause oscillations in the ionization rate such that each region where r_s has decreased corresponds to an increase in $-dn_p/d\xi$. Eventually, the plasma density is sufficiently large that the latter portion of the optical pulse is defocused. In the region where the pulse is sufficiently defocused the ionization rate falls, $dn_p/d\xi \simeq 0$, and an ionization front develops which propagates toward the front of the beam at the disruption velocity v_d, see Eq. (43). This can be seen in Fig. 12(c), where the ionization front is at $\xi \simeq -42$ μm, and in Fig. 12(d), where the ionization front is at $\xi \simeq -29$ μm.

The growth of the perturbed radius due to the instability is plotted versus ξ at fixed $\eta = 75$ cm in Fig. 13(a), where $\ln|\Delta r|$, from the integration of the envelope equation, Eq. (52), is compared to the number of e folds N_e from Eq. (58). Here, $\Delta r = (r_s - r_{s0})/r_{s0}$, where $r_s(\xi)$ is plotted in Fig. 12(c). Similarly, growth versus $\eta = z$ at fixed $\xi = -40$ μm is shown in Fig. 13(b). For both plots, good agreement is obtained between the slope of $N_e(\xi)$ and the peaks of the $\ln|\Delta r|$ curve. As expected, agreement tends to break down for $\xi, \eta \to 0$, where the growth is not yet in the asymptotic limit, and for $\ln|\Delta r| \to 0$, where the growth is nonlinear.

V. SELF-GUIDED INVERSE CHERENKOV ACCELERATOR

A. Electron energy gain in vacuum

The axial field component of a higher-order radially polarized optical beam, which has an amplitude on axis of $E_{z0} \simeq (2\sqrt{2}/kr_s)E_0$, can be used to accelerate an injected electron beam propagating along the z axis [9,40–43]. In vacuum, the phase velocity v_{ph} of the optical beam is greater than c and near the focal point is $v_{ph}/c \simeq 1 + 2/kZ_{R0}$. Since $v_{ph} > c$, phase slippage between the electrons and optical beam will occur. For a highly relativistic injected electron in vacuum, the slippage distance L_s is defined as the distance over which the electron phase slips by one-half an optical period, $L_s(v_{ph} - c)/c \simeq \lambda/2$, which gives $L_s \simeq \pi Z_{R0}/2$. It can be shown that a highly relativistic electron interacting with the axial optical field E_z in vacuum, Eq. (59), from $z = -\infty$ to $z = \infty$ experiences zero net energy gain. This result is a particular case of the Lawson-Woodward theorem [44,45].

It can also be shown [9,38–43], however, that if the interaction distance is limited by placing a mirror approximately one Rayleigh length from the focal point, i.e., $-Z_{R0} \lesssim z \leq \infty$, then the maximum energy gain for a highly relativistic electron is $W_e[\text{MeV}] \simeq P^{1/2}[\text{GW}]$. Material damage considerations, associated with the introduction of an optical component near focus, place serious limits on the optical intensity [9,42].

B. Electron energy gain in the conventional ICA

By introducing a neutral gas into the interaction region, as in the inverse Cherenkov accelerator (ICA), the phase velocity of the optical beam can be reduced and phase slippage reduced. In the conventional ICA [6–8], the optical beam diffracts and the effects of nonlinear self-focusing and ionization are neglected. For a higher-order Gaussian beam the
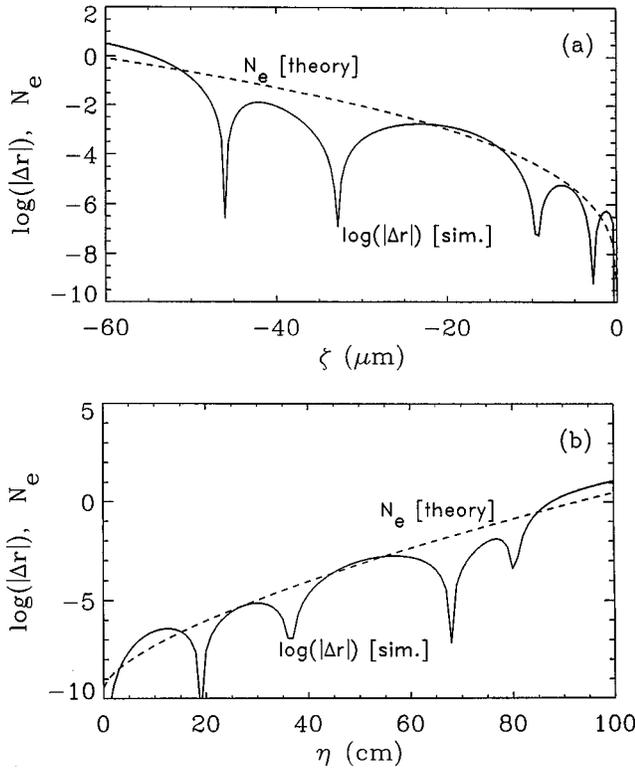
FIG. 13. Perturbed radius $\ln|\Delta r|$ (solid line) and number of e folds N_e (dashed line) plotted (a) versus ξ at fixed $\eta=z=75$ cm and (b) versus z at fixed $\xi=-40$ μm. Here, $\Delta r=(r_s-r_{s0})/r_{s0}$ is determined from the time integration of the envelope equation, Eq. (52), while N_e is given by Eq. (58). Note that log is the natural logarithm to base e, i.e., ln.

phase velocity near focus is $v_{ph}/c\simeq 1+2/kZ_{R0}-(n_0-1)/n_0$. Typically $n_0-1\ll 1$ and is proportional to the neutral gas density n_{n0}. Proper choice of n_{n0} can result in $v_{ph}\lesssim c$ and the reduction of phase slippage; however, diffraction remains an important limitation.

The energy gain in a conventional ICA driven by a higher-order Gaussian beam can be calculated as follows. Assuming vacuum diffraction and neglecting nonlinear and plasma effects, the axial electric field along $r=0$ in the conventional ICA is given by

$$E_z(r=0)=-E_{z0}(1+z^2/Z_{R0}^2)^{-1}\sin\psi, \qquad (59)$$

where $E_{z0}=(2\sqrt{2}/kr_{s0})E_0(z=0)$ is the peak axial electric field, $\psi=kz-ckt/n_0-2\tan^{-1}z/Z_{R0}+\psi_0$ is the phase, and ψ_0 is a constant. Equation (59) follows from Eq. (45) with $E_0(\xi,\eta)=E_0(\xi,\eta=0)r_{s0}/r_s(\eta)$, where $r_s=r_{s0}(1+\eta^2/Z_R^2)^{1/2}$ and $\eta=z$. The energy gain of a highly relativistic electron interacting with the optical field, given by Eq. (59), in a medium with linear refractive index n_0 is given by

$$W_e=q\int_{-\infty}^{\infty}dz\,E_z(r=0)=-2\pi qE_{z0}\Delta kZ_{R0}^2\exp(-\Delta kZ_{R0}),$$
$$(60)$$

for $\Delta k\geq 0$ and $W_e=0$ for $\Delta k<0$, where $\Delta k=k(n_0-1/\beta_0)/n_0\simeq k(n_0-1-1/2\gamma_0^2)/n_0$, $\gamma_0=(1-\beta_0^2)^{-1/2}$ is

the electron relativistic mass factor, $\beta_0=v_0/c$, v_0 is the axial electron velocity, and an initial phase of $\sin\psi_0=1$ was assumed. In obtaining Eq. (60) the electron trajectory was taken along $r=0$ from $z=-\infty$ to $z=\infty$, where $z=\beta_0ct\simeq ct(1-1/2\gamma_0^2)$. Equation (60) is valid as long as the energy gain is less than the initial energy, $W_e\ll(\gamma_0-1)mc^2$. For highly relativistic electrons in vacuum ($\beta_0=1$ and $n_0=1$), Δk vanishes and the energy change is zero, $W_e=0$, in accordance with the Lawson-Woodward theorem. In a gas, the energy gain W_e is maximum when $\Delta kZ_{R0}=1$, i.e., when $n_0-1=n_0/kZ_{R0}+1/2\gamma_0^2=\frac{1}{2}[(\lambda/\pi r_s)^2/n_0+1/\gamma_0^2]$. In this case, the maximum energy gain in the conventional ICA is given by

$$W_{max}=-qE_{z0}(2\pi/e)Z_{R0}=-qE_0(0)(2\sqrt{2}\pi/e)r_{s0}. \quad (61)$$

The maximum energy gain is the product of the peak axial field E_{z0} and $(2\pi/e)Z_{R0}$, which is the effective acceleration length. In terms of the optical power, Eq. (61) can be written as

$$W_{max}[\text{MeV}]=2.3P^{1/2}[\text{GW}]. \qquad (62)$$

A similar result can be obtained in vacuum acceleration by limiting the interaction region to approximately $2Z_R$ about the laser focus through the use of optical components (e.g., mirrors).

In addition to the higher-order Gaussian optical beam discussed above, a conventional ICA could be driven by a first-order Bessel (axicon) beam [7,8]. A nonideal Bessel beam (finite transverse extent) consisting of N rings (lobes) will propagate a distance $L_{max}\cong NZ_{R0}$, where $Z_{R0}=kr_0^2/2$ and r_0 is the width of an individual ring. Consequently, the maximum energy gain in a conventional ICA driven by a Bessel beam is approximately a factor of $N^{1/2}$ greater than an ICA driven by a higher-order Gaussian beam, assuming equal total power in each of the beams, as discussed in Appendix D.

The above calculation of the energy gain in the conventional ICA assumes vacuum diffraction, i.e., the effects of nonlinear self-focusing and ionization are neglected. Equation (60) only holds for powers below the nonlinear focusing power, $P\ll P_{NR}$, and intensities below the ionization threshold, $I\ll I_I$. Typically, at atmospheric pressures, $P_{NR}\sim 10$ GW (1 TW) for a $\lambda=1$ μm (10 μm) laser, the single-stage energy gain in a conventional ICA driven by a higher-order Gaussian beam, Eq. (62), is limited to $W_e\sim 5$ MeV (50 MeV). Higher energy gains require higher laser power, and the effects of self-focusing and ionization can no longer be neglected. Recent experiments at Brookhaven National Laboratory [8] on the conventional ICA observed a 3.7 MeV energy gain (31 MeV/m) of an injected electron beam (40 MeV) using a 580-MW CO_2 laser ($\lambda=10.6$ μm) in 2.2 atm of H_2 gas.

C. Electron acceleration in the self-guided ICA

To enhance the single-stage energy gain, a self-guided ICA configuration is proposed and analyzed. The self-guided ICA operates at laser powers near the nonlinear focusing power and intensities near the ionization intensity. The self-guided ICA is based on the optically guided higher-order radially polarized optical beam described in Sec. IV. The energy gain is enhanced since (i) the self-guided ICA oper-

ates at higher power and intensity which increases the accelerating field, and (ii) the optical beam is self-guided, which increases the acceleration length beyond the limits of vacuum diffraction.

1. Phase velocity

The evolution of the spot size of the higher-order radially polarized beam in the self-guided ICA is described by Eq. (52). In addition, the evolution of phase velocity $v_{ph} = c\beta_{ph}$ of the higher-order radially polarized beam is given by Eq. (22d) with $p=1$ together with Eqs. (47) and (51),

$$\beta_{ph} \simeq n_0^{-1} + 4(n_0 k^2 r_s^2)^{-1}$$
$$\times \left[1 - \frac{3}{2} \frac{P}{P_{NR}} + \frac{1}{8} r_s^2 k_{p0}^2 (\sigma_{R1} + 2\sigma_{R2}) \right], \quad (63)$$

where the terms on the right-hand side denote, respectively, the contributions from the linear refractive index, finite spot size, nonlinear refractive index, and the plasma. For a self-guided beam with $r_s = r_{s0}$, the phase velocity is $\beta_{ph} < 1$ and given by

$$\beta_{ph} \simeq [1 - 0.5(\lambda/\pi n_0 r_{s0})^2 P/P_{NR}] n_0^{-1}. \quad (64)$$

The Lorentz factor associated with β_{ph} is $\gamma_{ph} = (1 - \beta_{ph}^2)^{-1/2}$,

$$\gamma_{ph} \simeq [(\lambda/\pi n_0^2 r_{s0})^2 P/P_{NR} + 1 - n_0^{-2}]^{-1/2}. \quad (65)$$

The nonlinear refractive index n_2 can have a significant contribution to the phase velocity.

The phase velocity can be controlled by introducing a small amount of background plasma. A transversely uniform background plasma will increase the phase velocity but have no effect on the focusing of the optical beam. By introducing a background plasma, the right-hand sides of Eqs. (63)–(65) will be modified by the addition of the term $k_{pb}^2/2k^2$, where $k_{pb}^2 = 4\pi q^2 n_b/mc^2$ and n_b is the background plasma density. The background plasma can be created by introducing a small concentration of easily ionized gas, i.e., a gas with a low ionization energy U_I. In addition, the background density can be tapered as a function of z to increase the phase velocity and optimize electron acceleration.

2. Accelerating gradient

In the self-guided ICA, the accelerated electrons are acted on by both an axial accelerating E_z field as well as a transverse E_r field (for $r \neq 0$). For an electron near the axis, $r^2/r_s^2 \ll 1$, the field components associated with the higher-order radially polarized mode are given by $E_z \simeq -(2\sqrt{2}/kr_s)E_0 \sin\psi$ and $E_r \simeq (\sqrt{2}r/r_s)E_0 \cos\psi$, where $\psi \simeq k\xi + \theta_0$ is the phase, as given by Eqs. (44) and (45). For $E_0 > 0$ the electron will experience axial acceleration within the phase regions $\sin\psi > 0$ and transverse focusing within the phase regions $\cos\psi < 0$. Simultaneous acceleration and transverse focusing occurs for $\pi/2 < \psi + 2\pi n < \pi$, where $n = 0, \pm 1, \pm 2, \dots$.

The accelerating gradient $E_{z0} = (\sqrt{2}/\pi)(\lambda/n_0 r_{s0})E_0$ can be estimated by considering the case of a self-guided beam and assuming that the peak intensity is near the ionization intensity I_I ($\sim 10^{14}$ W/cm^2) and that the power is near the nonlinear focusing power, i.e., $I_P \simeq I_I$ and $P \simeq P_{NR}$.

For this case we find that $E_0 \simeq (8\pi e I_I/cn_0)^{1/2}$, $\lambda/r_s \simeq (\pi/2)(en_0 n_2 I_I)^{1/2}$, and the accelerating gradient becomes

$$E_{z0} \simeq (en_2 I_I/2n_0)^{1/2} E_0 \simeq (2e/n_0)(\pi n_2 I_I/c)^{1/2} I_I^{1/2}, \quad (66)$$

which is a function of only n_2 and I_I. For the equilibrium in Fig. 11, $E_{z0} \simeq 450$ MeV.

VI. IONIZATION AND COLLISIONAL LOSSES

In this section the attenuation length of the optical field due to electron collisions and ionization losses is obtained by solving the wave equation, Eq. (1), in the one-dimensional limit in the absence of the nonlinear polarization field **P**. Collisions and ionization losses enter the wave equation through the plasma current density $\mathbf{J}_p$.

In the presence of ionization and electron collisions, the equation for the plasma current density given by Eq. (5) is modified,

$$\partial \mathbf{J}_p/\partial t = (\omega_p^2/4\pi)\mathbf{E} - \nu_m \mathbf{J}_p, \quad (67)$$

where ν_m is the effective electron collision frequency for momentum transfer and is discussed in Appendix B. Since the optical frequency is large compared to the collision frequency, $\omega_0 \gg \nu_m$, Eq. (67) can be approximated by

$$\partial \mathbf{J}_p/\partial t \simeq (\omega_p^2/4\pi)(1 - i\nu_m/\omega_0)\mathbf{E}, \quad (68)$$

where $n_p \sim \omega_p^2$ is given by Eq. (9).

Using the field representation in Eq. (6), the one-dimensional wave equation in the ξ, η variables becomes

$$2(ik + \partial/\partial\xi)\partial\hat{\mathbf{E}}/\partial\eta = k_p^2(1 - i\nu_m/\omega_0)\hat{\mathbf{E}}, \quad (69)$$

where $ck_p = \omega_p(\xi)$ is the plasma frequency. Since $k \ll |\partial/\partial\xi|$ and $\nu_m/\omega_0 \ll 1$, Eq. (69) can be approximated by

$$\frac{\partial}{\partial\eta}\hat{\mathbf{E}} \simeq -i(\omega_0/c)[1 - i\nu_m/\omega_0 + (ic/\omega_0)\partial/\partial\xi](\widetilde{\omega}_p^2\hat{\mathbf{E}}/2), \quad (70)$$

where $\omega_0 = ck$, $\widetilde{\omega}_p = \omega_p(\xi)/\omega_0$ is the normalized plasma frequency, and $n_0 = 1$ has been assumed. Substituting $E = E_0 \exp(i\theta_0)$ into Eq. (70), where $E_0(\xi, \eta)$ and $\theta_0(\xi, \eta)$ are the real field amplitude and phase, we obtain

$$\partial E_0^2/\partial\eta \simeq -\Gamma(\xi, \eta)E_0^2, \quad (71a)$$

$$\frac{\partial\theta_0}{\partial\eta} \simeq -\frac{1}{2}\widetilde{\omega}_p^2(\omega_0/c)\left(1 + \frac{\eta}{2}\frac{\partial\widetilde{\omega}_p^2}{\partial\xi}\right), \quad (71b)$$

where

$$c\Gamma = \nu_m\widetilde{\omega}_p^2 - c\partial\widetilde{\omega}_p^2/\partial\xi - \frac{c}{2}\widetilde{\omega}_p^2\partial\ln(E_0^2)/\partial\xi \quad (72)$$

is the effective damping rate due to collisions and ionization. A similar result, i.e., Eq. (71), has been obtained in Ref. [30].

In Eq. (72), the first term $\nu_m\widetilde{\omega}_p^2$ represents losses due to collisions. The second term $-c\partial\widetilde{\omega}_p^2/\partial\xi = W\widetilde{\omega}_p^2 n_{n0}/n_p$ represents ionization losses due to the fact that an electron produced by ionization in the presence of an optical field leaves

behind a residual energy approximately equal to the oscillation energy ϵ_{os}. The ionization loss term can also be derived by equating the rate of loss of electromagnetic energy $-c\partial(E_0^2/8\pi)/\partial\eta$ to the rate at which electrons are being produced $-c\partial n_p/\partial\xi = Wn_{n0}$ multiplied by the average oscillation energy per electron $\epsilon_{os} = q^2E_0^2/2m\omega_0^2$, which gives $c\partial E_0^2/\partial\eta = -W\widetilde{\omega}_p^2(n_{n0}/n_p)E_0^2$. This expression for the ionization losses assumes that the oscillation energy is large compared to the electron ionization energy, $\epsilon_{os} > U_I$. The third term on the right-hand side of Eq. (72) represents the slippage of the optical beam envelope in the $\xi = z - ct$, $\eta = z$ frame since the group velocity $v_g < c$ in the presence of the plasma.

Three-dimensional effects can be approximated by introducing a filling factor f into Eq. (71a). The rate of decrease of optical beam power, due to collisions and ionization losses, is given by

$$\partial P/\partial\eta \simeq -P/L_d, \tag{73}$$

where

$$L_d = ck^2/(\nu_m k_p^2 + Wk_n^2)f \tag{74}$$

is the attenuation length. In Eq. (74), W is the tunneling ionization rate, $k_p = (4\pi q^2 n_p/mc^2)^{1/2}$, $k_n = (4\pi q^2 n_{n0}/mc^2)^{1/2}$, $f = \sigma_p/\sigma_L \ll 1$ is the filling factor, and σ_p (σ_L) is the transverse cross-sectional area of the generated plasma (laser). As an example, for $n_{n0} \simeq 2.7 \times 10^{19}$ cm^{-3} and $n_p/n_{n0} \simeq 10^{-4}$, $\nu_m \simeq \nu_{en} \simeq 7 \times 10^{12}$ sec^{-1} as discussed in Appendix B. Assuming $W/c \simeq 10^{-2}$ cm^{-1}, the attenuation distance is $L_d \simeq 10^3 f^{-1}$ cm.

The actual frequency of the optical beam is $\omega = -\partial(k\xi + \theta_0)/\partial t = ck + c\partial\theta_0/\partial\xi$. Using Eq. (71b) we find

$$\omega/\omega_0 \simeq 1 - \frac{\eta}{2}\partial\widetilde{\omega}_p^2/\partial\xi - \frac{\eta^2}{16}\partial^2\widetilde{\omega}_p^4/\partial\xi^2. \tag{75}$$

The third term on the right-hand side of Eq. (75) is typically small compared to the second term. Furthermore, since $\partial\omega_p^2/\partial\xi < 0$, the frequency will be upshifted as the optical beam propagates [29–31].

VII. DISCUSSION

The propagation of both fundamental and higher-order Gaussian optical beams in gases undergoing ionization has been studied analytically and numerically. The propagation model includes the effects of the linear and nonlinear polarization current, the linear plasma current, and plasma generation via tunneling ionization. Envelope equations describing the evolution of the spot size, amplitude, and phase of the optical beam were derived by applying the source-dependent expansion method to the paraxial wave equation in the r, $\xi = z - ct/n_0$, and $\eta = z$ coordinate system. The envelope equation for the evolution of the spot size r_s is given by Eq. (29) for the fundamental Gaussian beam or Eq. (52) for the higher-order radially polarized beam. The nonlinear focusing power for the high-order beam P_{NR} was found to be four times that of the fundamental Gaussian beam, i.e., $P_{NR} = 4P_{NG} = 2\lambda^2/(\pi n_0 n_2)$.

The evolution of an optical pulse with an initial power profile of the form $P(\xi) = P_0\sin^2(\pi\xi/L)$ for $-L \leq \xi \leq 0$ with $P_0 > P_N$ has been studied by numerically solving the envelope equation Eq. (29) [Eq. (52)], where $P_N = P_{NG}$ (P_{NR}) for the fundamental Gaussian (high-order radially polarized) beam. The front portion of the optical beam where $P < P_N$ diffracts up to the point where $P = P_N$. The point on the front of the optical beam where $P = P_N$ remains guided, $r_s \simeq r_{s0}$. A narrow region of the pulse just behind the position where $P \gtrsim P_N$ will focus. In the region where focusing occurs the intensity and the ionization rate increase, resulting in a sharp rise in the plasma density. The increase in plasma density causes the remainder of the pulse to diffract. This behavior is shown in Figs. 3, 4, and 12.

Self-guided solutions, i.e., $\partial r_s/\partial\eta = 0$, can result from a balancing of diffraction, nonlinear self-focusing, and plasma defocusing. These solutions are characterized by beam profiles with $P = P_N$ at the front ($\xi = 0$) of the beam, since the plasma density vanishes at the leading edge of the optical beam. As the plasma density increases behind the front of the beam ($\xi < 0$), the power in the self-guided beam also increases such that $P > P_N$ and $\partial P/\partial\xi < 0$. For a typical self-guided solution the amount of ionization is small, $n_p/n_{n0} \lesssim 10^{-4}$. Examples of self-guided beam profiles are shown in Figs. 5, 6, and 11.

Self-guided optical beams are subject to an ionization-modulation (IM) instability. The mechanism of the IM instability can be understood by considering a perturbation of the spot size δr for which the power is constant. For example, if the beam spot size is increased, i.e., $\delta r > 0$, the beam intensity and ionization rate are reduced, resulting in less plasma generation. Nonlinear self-focusing and plasma defocusing are no longer balanced and the beam focuses. The focusing beam overshoots its equilibrium value, i.e., $\delta r < 0$, some distance behind the front. When $\delta r < 0$, the intensity, ionization rate, and plasma density increase, causing the beam to defocus and again overshoot its equilibrium value. This focusing and defocusing of the beam due to a varying amount of ionization throughout the beam results in the IM instability. For a fundamental Gaussian beam, the asymptotic linear growth of the instability is given by $\delta r \sim \exp[(1 \pm i\sqrt{3})N_e]$, where $N_e \simeq [(k_{p0}r_{s0}\eta/Z_{R0})^2 n_p(\xi)/n_{n0}]^{1/3}$, as given by Eq. (42). The modulation amplitude increases with both the distance from the front of the beam, $|\xi|$, and the propagation distance $\eta = z$. The IM instability leads to a disruption (erosion) of the back of the beam which moves toward the beam front at a relative velocity v_d given by Eq. (43). Good agreement was obtained between numerical solutions of the full envelope equation for the IM instability in the linear regime and the analytical expressions for the asymptotic growth rates, as shown in Figs. 8 and 13.

The results in Sec. III show that self-guiding of a Gaussian beam requires a nearly constant axial power profile with $P \simeq P_{NG}$ and a peak intensity near the ionization threshold, $I_P \simeq I_I$. Recent experiments on the propagation of short (200 fs, $\lambda = 0.8$ μm) laser pulses in air have been performed at the University of Michigan [17]. In these experiments, a large portion of the initial laser power was observed to be confined to a narrow spot size (~ 40 μm) that propagated some 20 m in air at 1 atm. The intensity in the narrow filament was on the order of 10^{14} W/cm^2 and partial ionization was observed along the propagation axis. The laser pulse was injected into

air with a large spot size ($\sim$1 cm) and a peak power several times the nonlinear focusing power, $P \simeq 6P_{NG} \simeq 10$ GW, where $P_{NG} \simeq 1.7$ GW for air. These experimental conditions are far from the theoretical conditions for self-guiding a Gaussian beam, as found in Sec. III. Not only is the observed threshold for nonlinear focusing substantially higher than the calculated value, but a significant portion of the optical power is observed to reside in a large halo surrounding the central filament. This large radius ($\sim$1 cm) halo strongly affects the propagation dynamics. The present analysis does not directly apply to this experiment since the observed optical beam is apparently far from a Gaussian transverse profile.

In addition, a self-guided inverse Cherenkov accelerator (ICA) has been proposed and analyzed. In this accelerator configuration a self-guided higher-order radially polarized optical beam propagates through a gas. Associated with the high-order mode is an axial electric field component that is maximum along the axis and can be used to accelerate an injected electron beam. The phase velocity of the self-guided mode is less than the speed of light and can be controlled by introducing a uniform background plasma. Since the self-guided mode has a power near the nonlinear focusing power, $P \simeq P_{NR}$, the amplitude of the axial electric field can be written as $E_{z0} \simeq 9.6(n_2/c)^{1/2} I_p / n_0$, where I_p is the peak optical beam intensity. Large values of the axial field amplitude, typically on the order of 0.5 GV/m, require large values of n_2 and I_p. Since n_2 is proportional to the neutral gas density n_{n0}, the accelerating field can be increased by increasing n_{n0}. To avoid excessive amounts of plasma and defocusing, the peak intensity should be near the ionization threshold, $I_p \simeq I_I$. In the self-guided mode the propagation distance is limited by the IM instability. Since the number of e folds of the IM instability scales as $N_e \sim n_p^{1/3}$, where the plasma density n_p is a highly nonlinear function of I_p, the peak intensity must be kept sufficiently low.

ACKNOWLEDGMENTS

APPENDIX A: PHOTOIONIZATION RATES

Photoionization can take place in either the tunneling or multiphoton regime [24–28]. These regimes are characterized by the Keldysh parameter $\gamma_k = (U_I/\epsilon_{os})^{1/2}$, where U_I is the ionization energy and $\epsilon_{os} = \frac{1}{2}m(q|\hat{\mathbf{E}}|/m\omega)^2$ is the electron oscillation energy. The Keldysh parameter can also be written as $\gamma_k = \omega\tau_t$, where τ_t is the tunneling time, i.e., the transit time of the electron through the atomic Coulomb barrier. The low-field limit ($\gamma_k > 1$) corresponds to the multiphoton ionization regime, whereas the high-field limit ($\gamma_k < 1$) corresponds to the tunneling ionization regime.

In the high-field limit, $\gamma_k < 1$, the ionization rate can be determined by a tunneling calculation for an atom in the presence of a static electric field of amplitude E. The tunneling ionization rate, i.e., the probability (per unit time) of ionization, is given by [25]

$$W = 4\Omega_0 (\widetilde{U}_I)^{5/2} (E_H/E) \exp[-\tfrac{2}{3}(\widetilde{U}_I)^{3/2} E_H/E], \quad \text{(A1)}$$

where the variables in Eq. (A1) have been normalized in terms of atomic constants. In Eq. (A1), $\Omega_0 = \alpha_f c/a_0 = 4.1 \times 10^{16}$ sec^{-1} is the characteristic atomic frequency, $\alpha_f = 2\pi q^2/hc = 1/137$ is the fine-structure constant, $\alpha_f c$ is the characteristic atomic velocity, $a_0 = h^2/(4\pi^2 q^2 m) = 5.3 \times 10^{-9}$ cm is the Bohr radius, $\widetilde{U}_I = U_I/U_H$, U_I is the ionization energy in eV, $U_H = 13.6$ eV is the ionization energy of hydrogen, and $E_H = |q|/a_0^2 = 5.2$ GV/cm is the hydrogenic electric field. The ionization rate in Eq. (A1) vanishes at both small and large values of the electric field, and has a maximum at $E = 2.3(\widetilde{U}_I)^{3/2} E_H$.

In the limit $\gamma_k \ll 1$, the tunneling time is much less than the laser period, $\tau_t \ll \omega^{-1}$, and therefore Eq. (A1) describes the instantaneous ionization rate in the laser field. For a circularly polarized laser field of the form $\mathbf{E} = |\hat{\mathbf{E}}|[\cos(kz-\omega t)\hat{\mathbf{e}}_x + \sin(kz-\omega t)\hat{\mathbf{e}}_y]$, where $|\hat{\mathbf{E}}|$ is constant, the ionization rate is obtained by setting $E = |\hat{\mathbf{E}}|$ in Eq. (A1). For a linearly polarized laser field of the form $\mathbf{E} = |\hat{\mathbf{E}}| \cos(kz-\omega t)\hat{\mathbf{e}}_x$, the average ionization rate is obtained by averaging Eq. (A1) over a laser oscillation period. The average ionization rate for a linearly or radially polarized laser field is found to be given by

$$W = 4(3/\pi)^{1/2} \Omega_0 (\widetilde{U}_I)^{7/4} (E_H/|\hat{\mathbf{E}}|)^{1/2}$$
$$\times \exp[-\tfrac{2}{3}(\widetilde{U}_I)^{3/2} E_H/|\hat{\mathbf{E}}|]. \quad \text{(A2)}$$

When $\gamma_k > 1$, ionization occurs by a multiphoton process. In this case N_0 photons are required to increase the electron energy by the ionization energy U_I. For an electron ionized from the ground state to the continuum, the ionization rate can be approximated by

$$W \simeq A\omega N_0^{3/2} (2\gamma_k)^{-2N_0}, \quad \text{(A3)}$$

where A is a constant on the order of unity and N_0 is the smallest whole number for which $N_0 h\omega/2\pi = U_I$, i.e., N_0 is the number of photons required for ionization.

APPENDIX B: ELECTRON COLLISION FREQUENCY

As the electrons in the weakly ionized gas or plasma oscillate under the influence of the optical field, they collide with the background electrons, ions, and neutral atoms. The electron collision frequency for momentum transfer is

$$\nu_m = \nu_{ei} + \nu_{en}, \quad \text{(B1)}$$

where ν_{ei} (ν_{en}) is the electron-ion (electron-neutral) collision frequency. The electron-electron collision frequency does not contribute to ν_m because the momentum of any pair of colliding electrons and associated current (masses and charges are identical) are conserved. Electrons colliding with electrons will therefore be accelerated on average as if the collision frequency were zero. Electron-electron collisions, however, lead to thermalization of the electrons.

The electron-ion collision frequency is given by [46]

$$\nu_{ei} = 4 \times 10^{-6} \ln\Lambda_{ei} n_i Z^2 \epsilon_{os}^{-3/2} \ [\text{sec}^{-1}], \quad \text{(B2)}$$

where $\ln\Lambda_{ei}$ is the Coulomb logarithm (typically, $\ln\Lambda_{ei} \simeq 10$–20), Z is the ion charge state, n_i is the ion density

in units of cm^{-3} (n_iZ is the electron plasma density) and ϵ_{os} is the electron oscillation energy in units of eV.

The electron-neutral collision frequency is given by [33–35]

$$\nu_{en} = \langle v_e n_n \sigma_{en}(v_e) \rangle, \tag{B3}$$

where σ_{en} is the electron-neutral cross section, v_e is the electron velocity, and the brackets $\langle \rangle$ denote an averaging over the electron velocity distribution. The electron-neutral cross section is generally a complicated function of the electron velocity. At low electron velocities the cross section is hard-sphere-like and independent of velocity, $\sigma_{en} \simeq \sigma_0$, where $\sigma_0 \sim 10^{-15}$ cm^2 is the hard-sphere cross section. As the electron velocity approaches the characteristic atomic electron velocity, polarization scattering is the dominant process and $\sigma_{en} \propto 1/v_e$. The characteristic atomic electron velocity is $v_0 = \alpha_f c$, where $\alpha_f = 1/137$ is the fine-structure constant and the characteristic electron energy $mv_0^2/2 = 13.6$ eV. At substantially higher electron velocities the scattering becomes Coulomb-like and $\sigma_{en} \sim 1/v_e^4$. The electron-neutral collision frequency can therefore be estimated to be $\nu_{en} \simeq n_n \sigma_0 v_{os}$ for $v_{os} < v_0$ and $\nu_{en} \simeq n_n \sigma_0 v_0$ for $v_{os} > v_0$, where v_{os} is the electron oscillation velocity.

Typically, the electron-neutral collisions is the dominant collisional process in weakly ionized gases. As an example, consider the case where the neutral density is $n_{n0} = 3 \times 10^{19}$ cm^{-3} and the electron oscillation velocity is $v_{os} = qE_0/m\omega = 5 \times 10^{-3} c$ ($\epsilon_{os} = mv_{os}^2/2 = 6.3$ eV). For a linearly polarized laser of wavelength $\lambda = 1$ μm, these parameters correspond to a peak intensity of $I = 3.5 \times 10^{13}$ W/cm^2 and peak electric field amplitude of $E_0 = 1.6 \times 10^8$ V/cm. Taking $\sigma_0 \simeq 10^{-15}$ cm^2, Eq. (B3) yields an electron-neutral collision frequency of $\nu_{en} \simeq 7 \times 10^{12}$ sec^{-1}, i.e., an electron-neutral collision time of $\tau_{en} = \nu_{en}^{-1} \sim 140$ fsec.

If, for the same example, the gas is weakly ionized with $n_i = 10^{-3} n_{n0} = 3 \times 10^{16}$ cm^{-3} and the electron oscillation energy is $\epsilon_{os} = 6.3$ eV, the electron-ion collision frequency from Eq. (B2) for singly ionized gas ($Z = 1$) is $\nu_{ei} \simeq 8 \times 10^{10}$ sec^{-1}, i.e., an electron-ion collision time of $\tau_{ei} = \nu_{ei}^{-1} \simeq 13$ psec. For these parameters the electron-neutral collision frequency is much greater than the electron-ion collision frequency, $\nu_{en} \gg \nu_{ei}$.

As another example consider the case of a plasma in which all the atoms are singly ionized, i.e., $Z = 1$ and $n_i = n_{n0}$ is the initial neutral density. For a laser intensity of $I = 10^{18}$ W/cm^2 and wavelength $\lambda = 1$ μm, the oscillation energy is $\epsilon_{os} \simeq 0.2$ MeV. For a neutral density of $n_{n0} = 10^{19}$ cm^{-3}, the electron-ion collision frequency is $\nu_{ei} \simeq 4 \times 10^6$ sec^{-1} and $\tau_{ei} = \nu_{ei}^{-1} \simeq 250$ nsec.

APPENDIX C: RADIATIVE AND COLLISIONAL LOSSES ON ACCELERATED ELECTRONS

In an inverse Cherenkov or a laser-plasma accelerator, the accelerated electrons interact with both the background electrons and nuclei. This interaction results in a loss of electron beam energy as well as an increase in beam emittance. Accelerated electrons traveling through neutral gas or plasma are scattered by the atomic nuclei and emit bremsstrahlung. The emission of bremsstrahlung represents a loss in electron energy. In addition, a highly relativistic electron will lose energy due to collisions with atomic or plasma electrons.

The rate of change of energy of the accelerated electrons is given by

$$dW_e/dz = G_{acc} - G_{rad} - G_{col}, \tag{C1}$$

where $W_e = (\gamma - 1)mc^2$ is the electron energy, $G_{acc} = qE_z$ denotes the accelerating gradient and G_{rad} (G_{col}) denotes the radiative (collisional) energy loss. The rate of electron energy loss due to bremsstrahlung is [47,48]

$$G_{rad} \simeq -W_e/L_b, \tag{C2}$$

where

$$L_b = (\tfrac{16}{3} \alpha_f n_a Z_a^2 r_e^2 \ln\Lambda)^{-1}, \tag{C3}$$

is the radiation damping length. In Eq. (C3), n_a is the density of nuclei, Z_a is the atomic number, $\alpha_f = 2\pi q^2/hc = 1/137$ is the fine-structure constant, $r_e = q^2/mc^2 = 2.8 \times 10^{-13}$ cm is the classical electron radius, and Λ is a function of the maximum and minimum impact parameters. The choice of Λ depends on various factors, such as the electron energy range and electronic screening effects. For highly relativistic energies, $W_e \gg W_c$, where complete screening occurs, $\Lambda \simeq 233 Z_a^{-1/3}$. At lower energies, $W_e \ll W_c$, where screening can be neglected, $\Lambda \simeq \gamma$. The critical energy W_c defining these regimes is $W_c \simeq 192 Z_a^{-1/3} mc^2$ and typically $\ln\Lambda \sim 5$–10. In hydrogen ($Z_a = 1$) at 1 atm ($n_a = 5.4 \times 10^{19}$ cm^{-3}) the radiation damping length is $L_b \simeq 12$ km, where we have taken $\ln\Lambda = 5$.

For a highly relativistic electron, the energy loss due to collisions with atomic or plasma electrons is given by the Bethe formula [47,48],

$$G_{col} \simeq 4\pi n_e r_e^2 mc^2 \ln B, \tag{C4}$$

where $n_e = n_a Z_a$ is the total electron density and B is the ratio of the maximum to minimum impact parameter. The ratio of radiative energy loss, Eq. (C2), to collisional energy loss (C4) is

$$G_{rad}/G_{col} = \frac{\gamma Z_a}{323} \frac{\ln\Lambda}{\ln B} \simeq 1.4 \times 10^{-3} W_e[\text{MeV}]. \tag{C5}$$

For an electron traveling through hydrogen ($Z_a = 1$) gas or plasma the radiative energy loss term is larger than the collision loss for energies above 700 MeV.

In addition, accelerated electrons will undergo small-angle scattering off nuclei, which leads to an increase in the electron beam emittance. The normalized emittance of the electron beam is given by $\epsilon_n \simeq \gamma R \langle \theta^2 \rangle^{1/2}$, where R is the rms beam radius and $\langle \theta^2 \rangle^{1/2}$ is the rms divergence angle of the beam. The rate of growth in the mean square angle is given by

$$d\langle \theta^2 \rangle/dz = 16\pi Z_a(Z_a+1) n_a r_e^2 \gamma^{-2} \ln\Lambda, \tag{C6}$$

and the normalized emittance ϵ_n increases according to [48,49]

$$\frac{d\epsilon_n^2}{dz} = \gamma^2 R^2 d\langle \theta^2 \rangle/dz = R^2/L_s, \tag{C7}$$

where $L_s^{-1} = 16\pi Z_a(Z_a+1)n_a r_e^2 \ln\Lambda$. For hydrogen at 1 atm ($Z_a=1$, $n_a=5.4\times10^{19}$ cm^{-3}, and $\ln\Lambda=5$), $L_s\simeq470$ cm.

APPENDIX D: INVERSE CHERENKOV ACCELERATION WITH BESSEL (AXICON) BEAMS

In addition to the higher-order Gaussian optical beam discussed in Sec. IV, an inverse Cherenkov accelerator (ICA) could be driven by a first-order Bessel optical beam [7,8]. Both optical beams are axially symmetric, radially polarized, and have an axial field peaked along the z axis. Nonideal Bessel beams (finite in transverse extent) can be formed using axicon mirrors [38,39]. Both the nonideal Bessel beam and the higher-order Gaussian beam diffract, limiting the acceleration distance. For a fixed total optical beam power, however, the energy gain in an ICA can be substantially higher when driven by a Bessel optical beam as opposed to a higher-order Gaussian optical beam. Nonlinear self-focusing in the gas and the effects of ionization are neglected in the following.

The wave equation in the paraxial approximation for a radially polarized, axially symmetric field E_r propagating in a medium with linear refractive index n_0 is

$$\left[\frac{\partial^2}{\partial r^2} + \frac{1}{r}\frac{\partial}{\partial r} - r^{-2} + 2ik\left(\frac{\partial}{\partial z} + \frac{1}{v}\frac{\partial}{\partial t}\right)\right]\hat{E}_r = 0, \quad (D1)$$

where $E_r=\hat{E}_r(r,z,t)e^{i(kz-\omega t)}/2+$c.c., $\hat{E}_r$ is slowly varying in z and t compared with k^{-1} and ω^{-1}, $v=c/n_0$, $k=\omega/v$, $\omega=2\pi c/\lambda$ is the frequency, and λ is the vacuum wavelength. An exact solution to Eq. (D1) which maintains a constant transverse profile is

$$E_r=E_0 J_1(k_\perp r)\exp[i(k-\Delta k)z-\omega t]+\text{c.c.}, \quad (D2)$$

where J_1 is the Bessel function of the first kind of order unity, $\Delta k = k_\perp^2/2k$, $k_\perp$ is the transverse wave number, and E_0 is the radial field amplitude. The ideal Bessel field in Eq. (D2) (infinite in transverse extent) is nondiffracting [50] in the sense that the transverse profile remains constant. The power, however, contained within an ideal Bessel beam is infinite since $\int dr\, J_1^2(k_\perp r)r=\infty$ when integrated from $r=0$ to $r=\infty$. Associated with the radially polarized field in Eq. (D2) is the axial field

$$E_z=\frac{ik_\perp E_0}{k-\Delta k}J_0(k_\perp r)\exp[i(k-\Delta k)z-\omega t]+\text{c.c.} \quad (D3)$$

The axial accelerating field in Eq. (D3) is peaked along the z axis and has axial phase velocity $v_{\rm ph}=\omega/(k-\Delta k)$,

$$v_{\rm ph}\simeq v[1+(k_\perp v/\omega)^2/2], \quad (D4)$$

which can be less than c for $n_0>1+(k_\perp c/\omega)^2/2$, where it is assumed that $(k_\perp c/\omega)^2\ll1$.

The ideal Bessel beam consists of an infinite number of rings (lobes) extending radially to infinity and having a radial width of $r_0\simeq\pi/k_\perp$. Since the asymptotic form $(k_\perp r\gg1)$ for the Bessel function is $J_1(k_\perp r)\sim(2/\pi k_\perp r)^{1/2}\cos(k_\perp r-3\pi/4)$, the power in each ring is essentially the same. If the power in each ring is denoted by P_0, then the total power contained in a nonideal Bessel beam of a finite radial extent $R_{\max}$ is $P\simeq NP_0$, where $N=R_{\max}/r_0$ is the number of rings. In principle, the number of rings can be large, $N\gg1$. A nonideal Bessel beam consisting of N rings diffracts away sequentially starting with the outermost ring [51]. The outermost ring diffracts after a distance $\sim\pi r_0^2/\lambda$, the next ring diffracts after a distance $2\pi r_0^2/\lambda$, and so on until the innermost ring diffracts away after a distance $\sim N\pi r_0^2/\lambda$. Hence, the maximum propagation distance of a nonideal Bessel beam consisting of N rings of width r_0 is

$$L_{\max}\simeq NZ_{R0}, \quad (D5)$$

where $Z_{R0}=\pi r_0^2/\lambda$ is the Rayleigh length associated with the individual rings, assuming $n_0\simeq1$.

The maximum energy gain in the ICA driven by a nonideal Bessel beam is

$$W_{\max}=-qE_{z0}L_{\max}, \quad (D6)$$

assuming that the axial phase velocity is matched to the electron velocity, where $E_{z0}=(k_\perp/k)E_0$ is the axial accelerating field along the z axis given by Eq. (D3). The radial field amplitude in terms of the power within a ring is

$$E_0\simeq(2\pi/r_0)(P_0/cn_0)^{1/2}. \quad (D7)$$

Using Eqs. (D5) and (D7), the maximum energy gain from Eq. (D6), in terms of the total optical power, is $W_{\max}=C_0 N^{1/2}P^{1/2}$, where $C_0=-q\pi^2/(cn_0)^{1/2}$. In practical units,

$$W_{\max}(\text{MeV})=1.7N^{1/2}[P(\text{GW})]^{1/2} \quad (D8)$$

for an ICA driven by a nonideal Bessel beam. If a higher-order Gaussian optical beam of the same total power P were used instead of the nonideal Bessel beam, the maximum energy gain, Eq. (62), would be $W_{\max}(\text{MeV})=2.3[P(\text{GW})]^{1/2}$. The energy gain in the ICA is $\sim N^{1/2}$ times greater for a nonideal Bessel beam as compared to a higher-order Gaussian beam of the same total power.

The ratio of the accelerating gradient for the nonideal Bessel beam, E_{zB}, to that of the higher-order Gaussian beam, E_{zG}, is $E_{zB}/E_{zG}\sim N^{-1/2}(r_{s0}/r_0)^2$, where r_{s0} is the spot size for the higher-order Gaussian beam.

[1] *The Supercontinuum Laser Source*, edited by R. R. Alfano (Springer-Verlag, New York, 1989).

[2] P. B. Corkum, C. Rolland, and T. Rao, Phys. Rev. Lett **57**, 2268 (1986).

[3] J. F. Reintjes, *Nonlinear Optical Parametric Processes in Liquids and Gases* (Academic, Orlando, FL, 1984).

[4] A. L'Huillier, L. A. Lompre, G. Mainfray, and C. Manus, in *Atoms in Intense Laser Fields*, edited by M. Gavrila (Academic, San Diego, 1992), p. 139.

[5] N. H. Burnett and P. B. Corkum, J. Opt. Soc. Am. **6**, 1195 (1989); D. C. Eder *et al.*, Phys. Plasmas **1**, 1744 (1994).

[6] J. A. Edighoffer, W. D. Kimura, R. H. Pantell, M. A. Piestrup,

and D. Y. Wang, Phys. Rev. A **23**, 1848 (1981).

[7] J. R. Fontana and R. H. Pantell, J. Appl. Phys. **54**, 4285 (1983).

[8] W. D. Kimura, G. H. Kim, R. D. Romea, L. C. Steinhauer, I. V. Pogorelsky, K. P. Kusche, R. C. Fernow, X. Wang, and Y. Liu, Phys. Rev. Lett. **74**, 546 (1995); in *Advanced Accelerator Concepts*, edited by P. Schoessow, AIP Conf. Proc. Vol. 335 (American Institute of Physics, New York, 1995), p. 131.

[9] P. Sprangle, E. Esarey, and J. Krall, Phys. Plasmas **3**, 2183 (1996).

[10] T. Tajima and J. M. Dawson, Phys. Rev. Lett. **43**, 267 (1979).

[11] P. Sprangle, E. Esarey, A. Ting, and G. Joyce, Appl. Phys. Lett. **53**, 2146 (1988); E. Esarey, P. Sprangle, J. Krall, and A. Ting, Phys. Fluids B **5**, 2690 (1993).

[12] C. E. Clayton, K. A. Marsh, A. Dyson, M. Everett, A. Lal, W. P. Leemans, R. Williams, and C. Joshi, Phys. Rev. Lett. **70**, 37 (1993).

[13] Y. R. Shen, *The Principles of Nonlinear Optics* (Wiley, New York, 1984).

[14] R. W. Boyd, *Nonlinear Optics* (Academic, San Diego, 1993).

[15] P. W. Milonni and J. H. Eberly, *Lasers* (Wiley, New York, 1988), Chap. 18.

[16] S. A. Akhmanov, V. A. Vyloukh, and A. S. Chirkin, *Optics of Fentosecond Laser Pulses* (American Institute of Physics, New York, 1992).

[17] R. Rankin, C. E. Capjack, N. H. Burnett, and P. Corkum, Opt. Lett. **16**, 835 (1991).

[18] W. P. Leemans, C. E. Clayton, W. B. Mori, K. A. Marsh, P. K. Kaw, A. Dyson, C. Joshi, and J. M. Wallace, Phys. Rev. A **46**, 1091 (1992).

[19] S. C. Rae, Opt. Commun. **97**, 25 (1993).

[20] X. Liu and D. Umstadter, in *Shortwavelength V: Physics with Intense Laser Pulses*, edited by M. D. Perry and P. B. Corkum (Optical Society of America, Washington, D.C, 1993), Vol. 17, pp. 45–49.

[21] A. Braun, G. Korn, X. Liu, D. Du, J. Squier, and G. Mourou, Opt. Lett. **20**, 73 (1995).

[22] P. Sprangle, A. Ting, C. M. Tang, Phys. Rev. Lett. **59**, 202 (1987); Phys. Rev. A **36**, 2773 (1987).

[23] E. Esarey, J. Krall, and P. Sprangle, Phys. Rev. Lett. **72**, 2887 (1994); P. Sprangle, J. Krall, and E. Esarey, *ibid.* **73**, 3594 (1994).

[24] L. V. Keldysh, Zh. Eksp. Teor. Fiz. **47**, 1945 (1964) [Sov. Phys. JETP **20**, 1307 (1965)].

[25] L. D. Landau and B. M. Lifshitz, *Quantum Mechanics* (Pergamon, Oxford, 1977), Sec. 77.

[26] M. V. Ammosov, N. B. Delone, and V. P. Krainov, Zh. Eksp. Teor. Fiz. **91**, 2008 (1986) [Sov. Phys. JETP **64**, 1191 (1987)].

[27] T. P. Hughes, *Plasmas and Laser Light* (Wiley, New York, 1975), Chap. 5.

[28] S. August, D. D. Meyerhofer, D. Strickland, and S. L. Chin, J. Opt. Soc. Am. B **8**, 858 (1991).

[29] M. Lampe, E. Ott, W. M. Manheimer, and S. Kainer, IEEE Trans. Microwave Theory Tech. **MIT-25**, 556 (1977); M. Lampe, E. Ott, and J. H. Walker, Phys. Fluids **21**, 42 (1978).

[30] V. B. Gil'denburg, A. V. Kim, and A. M. Sergeev, Pis'ma Zh.

Eksp. Teor. Fiz. **51**, 91 (1990) [(JETP Lett. **51**, 104 (1990)]; V. B. Gil'denburg, A. V. Kim, V. A. Krupnov, V. E. Semenov, A. M. Sergeev, and N. A. Zharova, IEEE Trans. Plasma Sci. **21**, 34 (1993).

[31] E. Esarey, G. Joyce, and P. Sprangle, Phys. Rev. A **44**, 3908 (1991).

[32] C. E. Max, J. Arons, and A. B. Langdon, Phys. Rev. Lett. **33**, 209 (1974); P. Sprangle, C. M. Tang, and E. Esarey, IEEE Trans. Plasma Sci. **15**, 145 (1987).

[33] Ya. B. Zeldovich and Yu. P. Raizer, *Physics of Shock Waves and High-Temperature Hydrodynamic Phenomena* (Academic, New York, 1966), Chap. VI.

[34] Y. P. Raizer, *Gas Discharge Physics* (Springer-Verlag, Berlin, 1991), Chap. 2.

[35] M. A. Lieberman and A. J. Lichtenberg, *Principles of Plasma Discharges and Material Processing* (Wiley, New York, 1994), Chap. 3.

[36] A. Yariv, *Quantum Electronics* (Wiley, New York, 1989), Chap. 6.

[37] Y. Shimoji, A. T. Fay, R. S. F. Chang, and N. Djeu, J. Opt. Soc. Am B **6**, 1994 (1989).

[38] S. C. Tidwell, G. H. Kim, and W. D. Kimura, Appl. Opt. **32**, 5222 (1993).

[39] I. V. Pogorelsky, W. D. Kimura, and Y. Liu, in *Advanced Accelerator Concepts*, edited by P. Schoessow, AIP Conf. Proc. Vol. 335 (American Institute of Physics, New York, 1995), p. 419.

[40] J. A. Edighoffer and R. H. Pantell, J. Appl. Phys. **50**, 6120 (1979).

[41] E. J. Bochove, G. T. Moore, and M. O. Scully, Phys. Rev. A **46**, 6640 (1992); M. O. Scully and M. S. Zubairy, *ibid.* **44**, 2656 (1991).

[42] E. Esarey, P. Sprangle, and J. Krall, Phys. Rev. E **52**, 5443 (1995).

[43] P. Sprangle, E. Esarey, J. Krall, and A. Ting, Opt. Commun. **124**, 69 (1996).

[44] J. D. Lawson, Rutherford Laboratory Report No. RL-75-043 (unpublished); IEEE Trans. Nucl. Sci. **NS-26**, 4217 (1979); P. M. Woodward, J. IEE **93**, 1554 (1947).

[45] R. B. Palmer, in *Frontiers of Particle Beams*, Lecture Notes in Physics Vol. 296, edited by M. Month and S. Turner (Springer-Verlag, Berlin, 1988), p. 607; Part. Accel. **11**, 81 (1980).

[46] *NRL Plasma Formulary*, edited by J. D. Huba, Naval Research Laboratory Publication NRL/PU/6790-94-265 (U.S. GPO, Washington, D.C., 1994).

[47] J. D. Jackson, *Classical Electrodynamics* (Wiley, New York, 1975), Chaps. 13–15.

[48] S. Humphries, Jr., *Charged Particle Beams* (Wiley, New York, 1990), Chap. 10.

[49] B. Hafizi, P. Sprangle, and A. Ting, in *Advanced Accelerator Concepts*, edited by P. Schoessow, AIP Conf. Proc. Vol. 335 (American Institute of Physics, New York, 1995), p. 480.

[50] J. Durnin, J. J. Miceli, and J. H. Eberly, Phys. Rev. Lett. **58**, 1499 (1987).

[51] P. Sprangle and B. Hafizi, Phys. Rev. Lett. **66**, 837 (1991); B. Hafizi and P. Sprangle, J. Opt. Soc. Am. A **8**, 705 (1991).